Spring 2005

Carbon Nanotubes and Tungsten Oxide Nanorods: Synthesis and Applications

Bing Xiao
Old Dominion University

CARBON NANOTUBES AND TUNGSTEN OXIDE NANORODS: SYNTHESIS AND APPLICATIONS

by

Bing Xiao

B.S. in Semiconductor Physics and Devices, July 1990,
M.S. in Condensed Matter Physics, July 1993,
Sichuan University, P. R. China

A Dissertation Submitted to the Faculty of
Old Dominion University in Partial Fulfillment of the
Requirements for the Degree of

DOCTOR OF PHILOSOPHY

ELECTRICAL ENGINEERING

OLD DOMINION UNIVERSITY

May 2005

Approved by:

Dr. Sacharia Albin (Director)

Dr. Hani E. Elsayed-Ali (Member)

Dr. Mounir Laroussi (Member)

Dr. Alex Pothen (Member)

ABSTRACT

CARBON NANOTUBES AND TUNGSTEN OXIDE NANORODS: SYNTHESIS AND APPLICATIONS

Bing Xiao
Old Dominion University, May 2005
Director: Dr. Sacharia Albin

Synthesis and applications of two types of one-dimensional nanomaterials, carbon nanotubes (CNTs) and tungsten oxide nanorods, are investigated in this dissertation. Multi-walled CNTs have been successfully synthesized using two types of chemical vapor deposition (CVD) methods: microwave plasma enhanced CVD and atmospheric pressure thermal CVD. CNTs and their synthesis processes are characterized with various analysis techniques including scanning electron microscopy (SEM), transmission electron microscopy (TEM), Raman spectroscopy, and optical emission spectroscopy. Ultra-thin and high quality multi-walled CNTs are discovered in CNT films produced by MPCVD, which exhibit good field emission performance that is found to be dependent on the synthesis conditions, like the growth time and CH_4/H_2 flow ratio. CNTs grown by thermal CVD have similar field emission performance. Based on silicon surface micromachining techniques and thermal CVD method, a self-aligned method has been developed to fabricate CNT based gated field emitter arrays (FEAs) which demonstrate low turn-on voltage and good emission current. Tungsten oxide nanorods have been synthesized on various tungsten substrates via thermal annealing in argon at atmospheric pressure. Nanorod growth mechanism is proposed based on thermal oxidation of tungsten in gas ambient with a very low partial pressure of oxygen as well as the self-catalytic effect on tungsten surface. The lattice structure and composition of the tungsten oxide nanorods are

observed and analyzed using high resolution TEM, selected area electron diffraction (SAD), and energy dispersive X-ray spectroscopy (EDXS). The analysis results reveal that the lattice structure of the tungsten oxide nanorods is closest to that of the monoclinic WO_3 crystal. Tungsten oxide nanorods have been successfully grown on tungsten tips for use in scanning tunneling microscope (STM) as probes which readily produce atomic resolution images on sample surface. Nanorod based FEAs are also successfully fabricated using similar techniques as those for fabricating CNTs based FEAs. Low turn-on voltage and low gate current are achieved.

.

ACKNOWLEDGMENTS

I would like to sincerely thank Dr. Sacharia Albin for his guidance and inspiration throughout this dissertation research. He brought me into the wonderful research world of microelectronics and nanotechnology. He contributed his knowledge, experience, and time to help me to bring this research to a conclusion.

I also want to thank Dr. Hani E. Elsayed-Ali, Dr. Mounir Laroussi, and Dr. Alex Pothen for their willingness to serve on my dissertation committee. Their precious comments and suggestions are greatly appreciated.

During my time on this research work, I obtained much help from my colleagues at the Microelectronics Laboratory and the Photonics Research Laboratory at Old Dominion University. I would especially like to thank Dr. Weihai Fu, Dr. Shangping Guo and Mr. Feng Wu for their help and advice, which makes my life much easier as a foreign student. I would also like to thank Dr. James Howe at University of Virginia for his precious support and advice to my dissertation research.

Finally, I would like to express my gratitude to my wife, Li Tao, and my families in China for their caring, understanding, and support of my life and studies.

TABLE OF CONTENTS

LIST OF TABLES

LIST OF FIGURES

Figure Page

CHAPTER I

INTRODUCTION

Nanomaterials are materials that have sizes in nanometer range in one, two, or three dimensions. Two dimensional nanomaterials have been studied extensively and used to fabricate optoelectronic and microelectronic devices, like quantum well lasers and high electron mobility transistors (HEMTs). Free standing two dimensional materials are commonly called nanosheets. One dimensional nanomaterials (also called quantum wires sometimes) are tiny tubes and rods whose diameters are within nanometer range, so they are also commonly named nanotubes, nanorods or nanowires. Unlike other nanomaterials, zero dimensional nanomaterials (also called quantum dots sometimes), like C_{60} and C_{70}, actually were discovered and extensively studied many years ago. Nanotubes and nanorods of many materials (metals, semiconductors, oxides, and carbon based materials) have been synthesized and some of them have demonstrated superb physical, chemical and mechanical properties. Therefore, nanotubes and nanorods have become important in nanomaterial researches. Zero dimensional nanomaterials are another active research area which may create fundamental changes in many scientific and technological fields.

Carbon nanotubes (CNTs) are a valuable one dimensional nanomaterial with many unique and useful properties which make them an excellent candidate for electron field emission material that is the key component for vacuum microelectronic devices which operate by electron field emission.

Tungsten based nanorods are newly discovered one dimensional nanomaterials

which have not been extensively studied for any applications. Therefore, tungsten oxide nanorods have been synthesized and investigated in this dissertation work for possible applications in vacuum microelectronic devices and as scanning tunneling microscope probes.

In this chapter, relevant work of vacuum microelectronics, CNTs, and tungsten based nanorods will be reviewed, based on which the motives of this dissertation work will be introduced.

1.1 Overview of Vacuum Microelectronics

1.1.1 Development of Vacuum Microelectronics

Vacuum microelectronics (VME) is the science and engineering of micrometer-scale vacuum electronic devices that use field emitters as the source of electrons. In contrast to the commonly used thermionic cathode where electrons are emitting from hot filaments, field emitter is one type of cold cathodes, which operates at room temperature and emit electrons under an electric field through a quantum mechanical tunneling process. This type of electron emission is called field emission. Compared with thermionic emission, field emission has some advantages, including instantaneous switching and response to field variation, resistance to temperature fluctuation and radiation, and a nonlinear current-voltage relationship where a small change of voltage can induce a large change of emission current.

However, field emission requires a very large electric field, more than 10^7 V/cm, to obtain a significant current. A traditional method to obtain this high field was to use a very sharp metal needle made by wet etching. Even so, high voltages of a few thousand of volts were still required to draw a meaningful current. Although more than 40 years

ago, Shoulders [1] presented a device concept which is exactly the VME device that we are now studying, it took almost a decade to have the first field emitter array successfully fabricated by Spindt [2] in 1968. By the middle of 1980's, a worldwide interest surged in field emitter arrays (FEAs) and their applications. In 1992, a new discipline named Vacuum Microelectronics was first proposed by Brodie and Spindt [3]. Now VME is still an active research field full of potential applications, like cold electron source, flat panel display [4], micro-sized vacuum electronic device [5], and microwave device [6].

1.1.2 Status of Field Emitter Arrays (Non-CNT Based)

A field emitter array is the foundation of vacuum microelectronic devices. It is a fruitful combination of the field emission cold cathodes and the micro-fabrication techniques, and it is believed to be capable of overcoming most of the drawbacks associated with the traditional vacuum tubes.

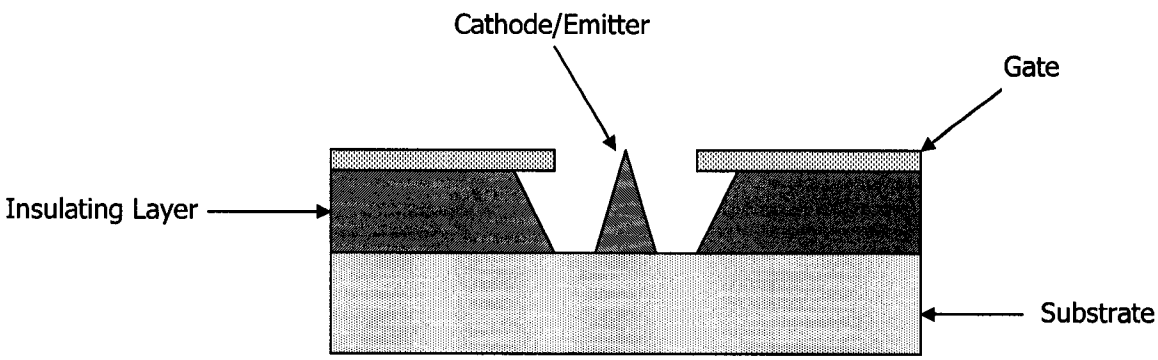

Fig. 1.1 Schematic diagram of a field emitter with gate.

FEAs can be fabricated by many methods, but most of their structures are rather the same. The structure of a typical FEA is shown in Fig.1.1. By using the micro-fabrication

and thin film deposition techniques, a tiny pyramid (or cone) cathode and a small circular gate hole can be made and the cathode-gate spacing can be less than 1 μm. The tiny cathode pyramid, with a typical height less than 2 μm, generally has a very sharp tip of radius in the nanometer range. The cathode materials could be metal [2], semiconductor [7,8], metal or semiconductor tip coated with diamond [9,10], or even reversely biased pn junction [11] operating in avalanche mode. The most advanced FEA [12] now has a tip-to-tip distance of 0.32 μm, and a tip density of $10^9/cm^2$. In MIT Lincoln Laboratory, an emission current of 1 μA (1 nA/tip or 1 A/cm^2) was measured at 25 V from an uncesiated 10 × 10 μm array of 900 tips; this is a record low gate voltage for FEAs. The cesiated array achieved 1μA at an even lower voltage of 10 V, and the maximum current density reached 1600 A/cm^2, again a record for FEAs. Spindt [13] reported a 5000-tip FEA yielded a total current of 100 mA, which corresponded to 20 μA/tip.

1.2 Overview of Carbon Nanotubes

1.2.1 Structures and Properties of Carbon Nanotubes

Carbon nanotubes were first discovered by Ijima in 1991 [14], and now are considered the most viable candidate to dominate the upcoming revolution in nanotechnology. Many potential applications have been proposed for carbon nanotubes, such as conductive and high-strength composite materials, energy storage, energy conversion, sensors, hydrogen storage, field emission devices, scanning probes, nanometer-sized electronic devices and interconnects. Some of these applications have been realized while most of them are still under development.

In terms of the thickness of the tube wall, there are two types of carbon nanotubes that have similar properties. Single-walled nanotubes (SWNTs), typically a few

nanometers in diameter, consist of a single graphite sheet rolled into a seamless cylindrical tube, while multi-walled nanotubes (MWNTs) can be viewed as a number of SWNTs that are concentrically arranged like the rings in a tree trunk. The tube diameters of MWNTs have a large variation within the range from a few nanometers to several hundred nanometers.

Unlike a single sheet of graphite, which is a semiconductor with zero band gap, SWNTs can be either metallic (conductive) or semi-conductive, depending on the direction in which the graphite sheet is rolled to form a nanotube. In order to define the different structures of SWNTs, a pair of integers (n, m), which are the two coefficients for the two base vectors in the lattice of a graphene layer, is introduced to denote the rolling direction and tube diameter [15]. Depending on the chirality (rolling direction), SWNTs are classified into three types, armchair ($n = m$), zig-zag ($n = 0$ or $m = 0$) and chiral (any other n and m). Nanotubes with $n - m = 3k$, where k is an integer, are metals, and all other nanotubes are semiconductors with a band gap that inversely depends on the nanotube diameter. Therefore, all armchair nanotubes are metals.

The electronic properties of MWNTs are similar to those of SWNTs, because the coupling between the walls is weak in MWNTs. Due to their extremely small diameters, carbon nanotubes are almost a perfect example of one-dimensional electronic materials (quantum lines) that are very useful in metaphysics and nano-electronic device research. The electronic transport in metallic nanotubes is ballistic movement (i.e., without scattering) that can occur over long nanotube lengths. This property enables them to carry very large current without being damaged by ohmic heating [16,17]. Phonons (lattice vibration) can also propagate easily along nanotubes. As a result, the measured room

temperature thermal conductivity is even greater than that of natural diamond and the basal plane of graphite (both 2000 W/m·K) [18].

SWNTs also have excellent mechanical properties with a large Young's modulus and a high tensile strength that are quite close to those of silicon carbide nanorods. However, when light-weight structural materials are needed, SWNTs prevail over any other materials with the density-normalized modulus and strength being, respectively, ~19 and ~56 times that of steel wire and, respectively, ~2.4 and ~1.7 times that of silicon carbide nanorods [19].

1.2.2 Application of Carbon Nanotubes in Field Emission

Despite their relatively high work function (~5.0 eV for graphite), carbon nanotubes have many remarkable physical and chemical properties that are suitable for field emission applications, and that is the reason why carbon nanotubes based field emission devices have been extensively studied. Generally, carbon nanotubes can provide stable emission, long lifetime, and low threshold field/voltage. Both SWNTs and MWNTs have been used as cold electron sources for flat panel displays [20], fluorescent lamps [21], gas discharge tubes for surge protection [22], portable x-ray sources [23], and microwave generators [24].

Carbon nanotubes have large field enhancement at the tips because of their large aspect ratios and small tube diameters, and low threshold field has been achieved for nanotube emitters. Carbon nanotubes' high thermal conductivity, high current-carrying capacity, and robust structure are ideal for long-term, high emission current density use. Unlike silicon and metal tips, carbon nanotubes do not have nonvolatile surface oxide that is a key factor to their stable field emission. Surface oxide can increase the work

function, impedes electron transport, and makes the effective work function changing during emission. Moreover, surface oxide could be the major cause for the field emitter destruction by trapping charge which could lead to arcing. Due to their stable chemical properties, carbon nanotube emitters can operate in moderate vacuum (10^{-8} Torr) instead of a vacuum of 10^{-10} Torr required by metal emitters.

1.3 Overview of Tungsten Based Nanomaterials

Tungsten (W) based nanomaterials (such as W, WO_x, and WC_x) are a new discovery in nanomaterials. Only a limited number of research reports have been published, and they mainly cover the synthesis and some very basic information about the morphologies and structural properties of those nanomaterials. No specific applications have been explored except STM probes.

1.3.1 Synthesis of Tungsten Based Nanometerials

Almost a decade ago, Dai *et al* [25] proposed that carbide nanorods could be prepared by reacting carbon nanotubes with volatile transition metals (including W) and their main group oxides and halides at high temperatures. However, no research work has been reported on synthesizing tungsten carbide nanorods based on their suggestion. Recently, W based nanomaterials have been synthesized using thermal annealing of metallic tungsten or tungsten compounds. Arie *et al* [26] synthesized tungsten carbide (WC) nanorods on nickel-coated tungsten tips through a catalytic CVD process using benzene. Nickel was used as the catalyst for dehydrogenation of benzene. Zhu *et al* [27] reported a simple annealing method to synthesize tungsten oxide nanomaterials. In their experiment, a tungsten foil covered with SiO_2 plate was annealed in Ar ambient at 1600 °C to produce micrometer scale tree-like structures that consisted of well-crystallized

nanoneedles and nanoparticles of various tungsten oxide phases. Subsequently, Lee *et al* [28] successfully produced single-crystalline W nanorods on sputtered W thin film. They annealed the substrate at 850 °C for a few minutes in a low pressure gas mixture of H_2 and Ar. The electron field emission properties of the tungsten nanorods were also measured. Meanwhile, Gu *et al* [29] obtained tungsten oxide nanorods on W tips and plates by heating them in Ar flow at normal pressure. Very recently, more results of tungsten-based nanomaterials have been published. Wang *et al* [30] successfully synthesized tungsten subcarbide (W_2C) nanorods on sputtered WC_x films using thermal annealing in nitrogen. The self-catalytic growth of W_2C nanorods was believed to be due to the formation of α-W_2C phase caused by carbon depletion in the WC_x films during thermal annealing. Lee *et al* [31] reported again that variously shaped tungsten nanostructures could be obtained using the same technique as reported before [28]. However, they also found that the morphology of those tungsten nanostructures was dependent on the residual stress and its spatial distribution across the tungsten film. Liu *et al* [32] showed that long and high quality tungsten oxide (WO_3) nanorods could be synthesized on tungsten hot filament in vacuum. This process involved an extended period (48 hrs) of annealing by self-heating during which room air was intentionally leaked into the vacuum chamber.

As for the growth mechanism of those W based nanomaterials obtained by simple annealing in gas ambient, a thorough understanding of it has not been achieved. However, it is generally believed that the synthesis of the W based nanomaterials through thermal annealing is due to the reaction between W and the trace amount of oxygen in the gas ambient. Vapor-solid model has been considered [29,33,34] for the growth

mechanism for tungsten oxide nanorods, and it is presumably caused by the formation of some volatile or mobile tungsten oxide phase and the self-catalytic effect at surface sites. Tungsten nanorods are believed to be created by reducing tungsten oxide in hydrogen.

1.3.2 Applications of Tungsten Based Nanomaterials

Metallic tungsten is an important material that has interesting properties for various applications, such as interconnects and gate electrodes in integrated circuits, high temperature diffusion barriers and corrosion resistant coatings, electron sources, and hot filaments. Nanomaterials have large surface area, and unusual mechanical, physical, and chemical properties, leading to a wide range of applications in both the conventional technology and the new nanotechnology. As for tungsten nanorods, they are good candidates for STM/AFM probes, electron field emission devices, electrodes in ion batteries, nano-electronic devices, and interconnects in ultra-large scale integrated circuits. Tungsten oxides are good electrochromic materials and could be used as semiconductor gas sensors. Tungsten oxide nanorods are generally conductive due to the extra electronic states induced by finite size effect, defects and impurities, as well as surface adsorbates. Tungsten carbides are conductive materials with high hardness, high melting point, and high resistance to oxidation and corrosion, which could make them very good candidates for STM/AFM tips and field emitters. Until now, W based nanorods have not been studied for their applications other than STM probes.

1.4 Motivation of Research

1.4.1 Field Emitter Arrays

Since the first FEA (Spindt cathode) was made in 1968, researchers have been searching for a perfect material for field emitters, but no material can meet all of the

requirements. Carbon nanotubes and W based nanorods are good candidates for this application.

However, incorporating CNTs into the FEA structure is not an easy task, because high quality CNTs are difficult to grow on common conductive substrates like silicon and most ordinary metals (except iron, cobalt, nickel, etc.), and it is also difficult to control the growth of CNTs (both in length, diameter and orientation) as well as maintaining gate material integrity at the high growth temperature. Therefore, a significant amount of research work still needs to be done to find optimum structures and processing methods in order to make the best use of CNTs for field emitters.

Until recently, the most commonly studied CNT emitters consist of a diode configuration without the gate, where the cathode is the CNTs, grown or placed on substrates, and positioned at a distance from the anode. Although low turn-on fields were measured, the voltages applied are still too high for many applications because the anode-cathode separations were usually large. In addition, gated emitters are preferred for many applications which include field emission displays, high-frequency amplifiers, high-voltage switches, portable x-ray sources, multi-beam electron-beam lithography, radiation and temperature-insensitive electronics, space craft propulsion, and electrostatic charge management.

To date, only a few studies on gated CNT FEA have been published [35,36], and two general approaches have been used for gating of CNT emitters. The first common technique involved the use of a CNT paste (CNTs mixed in a binding matrix) in conjunction with screen-printing or lithographic technique and the fabrication of the gate structures. All the gate diameters used in these studies were quite large (> 30 μm). The

threshold gate voltages vary from 20 V to 70 V. Most of the gate currents were either quite high or not reported.

Another common method uses *in situ* grown CNTs. Although high emitter density was achieved with this method, the published results did not show good performance for these devices. Most of them had very low emission currents and rather high threshold gate voltages, and some of the devices had large gate currents. The major reason for the poor performance of these CNT FEAs is that no high-quality (thin and vertically aligned) CNTs were uniformly grown in each gate hole (cavity) and the FEA structures were not optimized.

Untill now, W based nanomaterials have not been used in FEAs. Their performance is still unknown.

In this dissertation, the *in situ* method has been implemented for fabrication of CNT FEAs, and nanorod FEAs, which all have gated field emission structures for achieving improved performance with low turn-on voltage, higher emission current and low gate current.

1.4.2 STM Probes

Although W based nanorods are also good candidates for STM probes, only a few methods have been developed to fabricate STM probes with those nanomaterials. Current techniques need either sophisticated equipments or process, so the productivity is very low, which largely limits the application of those nanomaterial based STM tips. In order to make good use of the advantages of those nanomaterials, simple STM tip fabrication techniques are developed in this dissertation research, which can readily produce nanorod STM probes with good performance and low cost.

CHAPTER II

THEORIES

In this chapter, the principles of electron field emission and scanning tunneling microscopy will be discussed. Both problems have been theoretically investigated using quantum mechanics. The physical processes and major theoretical results of both problems will be described. As for nanotube and nanorod based field emitters, the important factors that affect the performance of those devices will be addressed. Similarly, important issues related to nanotube and nanorod based STM probes will be presented as well.

2.1 Electron Field Emission

Electron emission is defined as releasing of free electron from a solid surface of a substance caused by the external energy transferred to the electrons. Due to the surface potential barrier, electrons are unable to escape from the surface without the supply of additional external energy. The least amount of outside energy require by electron to emit from the solid surface is known as work function. The additional external energy required by the electron to emit from the solid surface could come from several sources which also determine the types of electron emission. The external energy can be thermal energy, energy stored in the electric field, photon energy or kinetic energy. Accordingly, there are four methods for obtaining electron emission from the solid surface.

2.1.1 Electron Emission Processes

The first type of electron emission is thermionic emission in which the additional energy supplied to the electron in the form of thermal energy that increases the

electron's kinetic energy. As a result, some electrons will obtain enough energy to jump over the surface potential barrier and escape into vacuum. A simple way to provide the energy is to heat the cathode to white hot so that electrons at the surface will gain enough thermal energy to achieve electron emission.

The second type of electron emission is called photoelectron emission (or photoelectric effect). In this type of emission the additional energy provided to cathode by photons. When a beam of light strikes the surface of the cathode, the energy from photons can be transferred to electrons within the cathode. If the energy from photons is greater than the work function the electrons may be excited and knocked out from the cathode surface. The emitted electrons are called as photoelectrons.

The third type of electron emission is the secondary electron emission in which the transfer of kinetic energy from high-energy electrons to electrons within cathode occurs when the cathode surface is bombarded by those high-energy electrons. If the energy of the striking particles is sufficient, the electrons at the cathode surface can be knocked out. For example, when electrons with energies of 10 to 1,000 electron volts strike a metal surface in a vacuum, their energy is lost in collisions in a region near the surface, and most of it is transferred to other electrons in the metal. Because this occurs near the surface, some of these electrons may be ejected from the metal and form a secondary emission current.

The last type of electron emission is the so-called field emission. Fowler and Nordheim first proposed this type of electron emission in 1928 based on the result from quantum mechanics [37]. They suggested that if an external field was strong enough, electrons could be extracted from the cathode surface into vacuum via quantum tunneling

through the surface barrier. It is because that the width and height of the surface barrier could be reduced due to the applied field and thus the probability of electrons tunneling through the barrier will increase accordingly, leading to the occurrence of electron emission. Unlike the other three types of electron emission, field emission actually requires no external energy supplied since electron tunneling process does not need any energy. The applied electric field is only used to reduce the barrier thickness and height and to pull electrons away from cathode surface. Both field emission and photoelectron emission need no thermal energy (heating) for electron emission. Therefore, the cathodes (electron sources) using those two types of electron emission are called cold cathode in contrast to hot cathode named for thermionic emission source. Due to the extremely high field (10^7 V/cm) required to extract the electron from the cathode, field emission devices usually are operating in high vacuum to prevent high field induced residual gas discharge.

2.1.2 Principles of Electron Field Emission

Field emission current is determined by the amount of available free electrons and the probability of these electrons tunneling through the cathode surface barrier. Therefore, electrons in the conduction band will be necessary for the field emission current. The conductivity of the cathode becomes important for providing the required electrons. According to the theory of quantum mechanics, the probability of an electron's tunneling through an energy barrier is decided by the electron's kinetic energy as well as the width of the energy barrier. It is well known that the height and width of surface barrier can be changed by external electric field, which is called Schottky effect. An approximated relation between the applied electric field F and the surface barrier width x_f at the Fermi

level could be expressed as [38]:

$$x_f = \frac{\phi}{eF} \tag{2.1}$$

where ϕ is the work function of the cathode, e is the electron charge. By increasing the applied field F, the energy barrier width x_f at the cathode surface can be effectively narrowed, enhancing the probability of electron tunneling.

To calculate field emission current density, let us assume s to be the kinetic energy of the electrons moving in the direction of the electric field at the surface. The emission current density can be written as [39]:

$$J = e\int_{-\infty}^{+\infty} N(T,s)D(F,s,\phi)ds \tag{2.2}$$

where $N(T,s)$ is the electron density at the surface and $D(F,s,\phi)$ is the probability for electrons with kinetic energy s to tunnel through the surface barrier, T is the temperature, F is the applied field, and ϕ is the work function of the cathode material.

From Eq. (2.2), the emission current can be regarded as a collection of all the possibly emitted electrons in the whole energy band. The electron density $N(T,s)$ depends not only on the kinetic energy of the electron but also on temperature. $N(T,s)$ is also called the supply function because it decides the amount of available electrons. $D(F,s,\phi)$ is called the transmission function since the amount of electrons that can be emitted depends on this probability.

The supply function can be derived by calculating all the states for conduction band electrons and the Fermi-Dirac probability of these states being occupied at temperature T. The result is quoted by Brodie [39] as:

$$N(T,s)=\left(\frac{4\pi mkT}{h^3}\right)\ln\left[1+\exp\left(\frac{s}{kT}\right)\right] \tag{2.3}$$

where m is the mass of the electron, h is Planck's constant, and k is Boltzmann's constant. At low temperature, $\exp(s/kT) >> 1$. Eq. (2.3) can be simplified as:

$$N(s)=\frac{4\pi ms}{h^3} \tag{2.4}$$

Eq. (2.4) shows that, at low temperature, the electron density at the cathode surface has no temperature dependence. For the electron emission at elevated temperatures, the emission current density needs to be modified by a factor, which is a function of temperature. This factor was given by Good and Muller as [40]:

$$J(T)=J(0)\frac{\pi kT/\alpha}{\sin(\pi kT/\alpha)} \tag{2.5}$$

where $J(0)$ is the emission current density at 0 K and α is given as:

$$\alpha=\frac{heF}{4\pi(2m\phi_0)^{1/2}t(y)} \tag{2.6}$$

with ϕ_0 as the work function at 0 K and $t(y)$ as a function of dimensionless variable y defined as:

$$y=\frac{(eF/4\pi\varepsilon_o)^{1/2}}{\phi'} \tag{2.7}$$

Here F is the applied field and ϕ' is the potential energy at distance d from the cathode surface. The distance d is defined as the distance from the cathode where the image charge effect starts to take effect. For most refractory cathode materials in their working range, $t(y)$ can be approximated as [41]:

$$t^2(y) = 1.1 \tag{2.8}$$

The actual temperature effect on the emission current density is quite weak for most metal cathodes. The equations for low temperature will be sufficiently accurate for cathodes operating below 1000 K [42].

The transmission function D can be described as similar to the electrons tunneling through a one-dimensional potential barrier. According to the results of analysis using quantum mechanics, the probability D of an electron tunneling through such a potential barrier is [38]:

$$D \approx \exp\left[-\frac{2(2m\phi)^{1/2} x_f}{h}\right] \tag{2.9}$$

where m is the electron mass, ϕ is the work function of the cathode, and x_f is the barrier width at Fermi level. Since the work function is dependent on the applied field, a new quantity, effective work function ϕ_{eff}, is introduced to include the field effect on work function, which can be expressed as:

$$\phi_{eff} = \phi - \left(\frac{e^3 F}{4\pi\varepsilon_o}\right)^{1/2} \tag{2.10}$$

where ε_o is the permittivity in vacuum. The change of surface barrier height and width at Fermi level under external electric field is given by Eqs. (2.1) and (2.10). Substituting ϕ_{eff} from Eq. (2.10) and x_f from Eq. (2.1) into Eq. (2.9), we get the tunneling probability D:

$$D \approx \exp\left(-\frac{2(2m_e\phi_{eff})^{1/2}\phi}{ehF}\right). \tag{2.11}$$

The detailed transmission function is given by Fowler and Nordheim as [37]:

$$D \sim \exp\left\{-\frac{4(2m\phi^3)^{1/2}}{3(\frac{h}{2\pi})eF}v(y)\right\} \tag{2.12}$$

where all the physical quantities are defined the same as previous descriptions except *v(y)*, which is a function with a variable *y* given in Eq. (2.7). For a good approximation, *v(y)* can be written as [41]:

$$v(y) = 0.95 - y^2. \tag{2.13}$$

Putting Eq. (2.4) and (2.12) into Eq. (2.2) yields the Fowler-Nordheim equation for field emission at low temperature:

$$J = \frac{e^3F^2}{8\pi h\phi t^2(y)}\exp\left[-\frac{8\pi(2m)^{1/2}\phi^{3/2}}{3heF}v(y)\right] \tag{2.14}$$

where *t(y)* and *v(y)* are the Nordheim elliptic functions of *y*. The numerical value of *t(y)* and *v(y)* were calculated by Good and Mueller. Eq. (2.14) was simplified by Spindt using approximations to Eqs. (2.8) and (2.13) and resulted in the following equation:

$$J = (\frac{1.5\times10^{-6}F^2}{\phi})\exp\left(\frac{10.4}{\phi^{1/2}}\right)\exp\left(\frac{-6.44\times10^7\phi^{3/2}}{F}\right). \tag{2.15}$$

From Eq. (2.15), it can be easily found that the emission current density is strongly affected by the work function of the cathode. As the cathode work function changes from 2 eV to 4 eV at a field of 10^7 V/cm, the emission current density changes nine orders of magnitude. Eq. (2.15) also clearly shows that the emission current density is strongly affected by the electric field strength. Therefore, in order to enhance field emission, a cathode with low work function and large field strength are required. However, since there are only a couple of choices for low work function conductors, increasing field

strength becomes a more feasible way to achieve high emission current.

In field emission experiments, the measurements of emission current and applied voltage generally produce the following relations: $J = I/\alpha$ and $F = \beta V$, where α is the emitting area and β is the field enhancement factor that accounts for the effects of both the separation of electrodes and the field enhancement due to the cathode geometric shape. Thus, the Fowler-Nordheim equation can be rewritten using current I and voltage V as [41]:

$$I = aV^2 \exp\left(-\frac{b}{V}\right) \tag{2.16}$$

where

$$a = \frac{1.56\times10^{-6}\alpha\beta^2}{1.1\phi}\exp\left(\frac{10.4}{\phi^{1/2}}\right) \tag{2.17}$$

$$b = 6.44\times10^{7}\phi^{3/2}/\beta \tag{2.18}$$

A plot of $\ln(I/V^2)$ versus $(1/V)$ will produce a straight line of slope $(-b)$ given the work function and field enhancement factor being constant during the emission measurement. The slope b is related to the work function of the cathode and the field enhancement factor as shown in Eq. (2.18). Since the plot is derived from the Fowler-Nordheim field emission equation, it is also called the F-N plot. If the F-N plot is not a straight line, it generally indicates some changes in the surface condition and geometry of the cathode or current being limited by available free electrons. For cathodes having the same geometry but different materials, a change in the slope of the F-N plot is a direct indication of the difference in the work function of the cathodes. On the other hand, for the same cathode

materials, a change in the slope corresponds to a change in the field enhancement factor β, which by definition is dependent on the separation between the anode (or gate) and the cathode as well as emitter geometry.

2.2 Scanning Tunneling Microscopy (STM)

2.2.1 Basics of STM

The scanning tunneling microscopy/microscope is the ancestor of all scanning probe microscopes. It was invented in 1981 by Gerd Binnig and Heinrich Rohrer at IBM Zurich [43]. Five years later they were awarded the Nobel Prize in physics for their invention. The STM was the first instrument to generate real-space images of surfaces with atomic resolution.

STM uses a sharpened, conducting tip with a bias voltage applied between the tip and the sample. The tip could be sharpened by the strong electric field which dislodges the surface atoms of the tip until only a few (ideally, one) remain. When the tip is brought within about 10Å of the sample surface (a distance comparable to spacing between neighboring atoms in the lattice), electrons from the sample begin to "tunnel" through the 10Å gap into the tip or vice versa, depending upon the sign of the bias voltage. The resulting tunneling current varies with tip-to-sample spacing, and it is the signal used to create an STM image. For tunneling to take place, both the sample surface and the tip must be conductive or semiconductive, unlike atomic force microscope which can also image on insulating surfaces.

The height and location of the STM tip are precisely controlled by a scanner that is made of piezoelectric materials which expand or contract when electric field is applied. The direction and the speed of the tip movement can also be accurately controlled by scanner. STM can operate in two modes which are constant-height mode and constant-current mode. In constant-height mode, the tip scans in a horizontal plane (no movement along the tip axis) above the sample surface and the tunneling current varies depending on topography and the local surface electronic properties of the sample. The tunneling current measured at each location on the sample surface constitutes the data set which can be the topographic image. In constant-current mode, STM uses feedback to keep the tunneling current constant by adjusting the height of the tip at each measurement point. For example, when the system detects an increase in tunneling current, it adjusts the voltage applied to the piezoelectric scanner to increase the distance between the tip and the sample. In constant-current mode, the motion of the scanner constitutes the data set. If the system keeps the tunneling current constant to within a few percent, the tip-to-sample distance will be constant to within a few hundredths of an angstrom. Each mode has advantages and disadvantages. Constant-height mode is faster because the system doesn't have to move the tip up and down, but it provides useful information only for relatively smooth surfaces. Constant-current mode can measure irregular surfaces with high precision, but the measurement takes more time.

As a first approximation, an image of the tunneling current maps the topography of the sample. More accurately, the tunneling current corresponds to the electronic density

of states at the surface. STM actually senses the number of filled or unfilled electron states near the Fermi surface, within an energy range determined by the bias voltage. Rather than measuring physical topography, it measures a surface of constant tunneling probability.

From a specific viewpoint, the sensitivity of STM to local electronic structure can cause trouble if one is interested in mapping topography. For example, if an area of the sample has been oxidized, the tunneling current will drop precipitously when the tip encounters that area. In constant-current mode, the STM will instruct the tip to move closer to maintain the set tunneling current. It may result in the tip digging a hole in the surface. From an optimist's viewpoint, however, the sensitivity of STM to surface electronic structure can be a tremendous advantage. Other techniques for obtaining information about the electronic properties of a sample detect and average the data originating from a relatively large area, a few microns to a few millimeters across. STM can be used as a useful surface analysis tool that probes the electronic properties of the sample surface with atomic resolution.

STM can also be used as a spectroscopy tool which is called scanning tunneling spectroscopy (STS) that studies the local electronic structure of a sample's surface. The electronic structure of an atom depends upon its atomic species (whether it is a gallium atom or an arsenic atom, for instance) and also upon its local chemical environment (how many neighbors it has, what kind of atoms they are, and the symmetry of their distribution).

STS encompasses many methods: taking "topographic" (constant-current) images using different bias voltages and comparing them; taking current (constant-height) images at different heights; and ramping the bias voltage with the tip positioned over a feature of interest while recording the tunneling current. The last example results in current vs. voltage (I-V) curves characteristic of the electronic structure at a specific location on the sample surface. STM can be set up to collect I-V curves at every point in a data set, providing a three-dimensional map of electronic structure. With a lock-in amplifier, dI/dV (conductivity) or dI/dz (work function) vs. V curves can be collected directly. All of these are ways of probing the local electronic structure of a surface using an STM.

Scanning probe microscopes can be operated in a variety of environments. The first STMs were operated primarily in UHV to study atomically clean surfaces. Silicon has been the most extensively studied material, and obtaining images of the 7 x 7 surface reconstruction of Si (111) is often used as a benchmark for evaluating the performance of UHV STM. A major application of UHV STM is STS. STS applied to atomically clean surfaces allows characterization of both topographic and electronic structure, without the added complication of contamination that is always present in air. Another application is the study of materials processes in-situ that is in the same vacuum environment in which the materials are grown. In this way, processing may proceed without contaminating the sample.

STM operation in air is difficult, since most surfaces develop a layer of oxide, H_2O or other contaminants that interfere with the tunneling current. One class of materials for which ambient STM works well is layered compounds. In graphite, MoS2, Nb3Se, and so forth, a clean, "fresh" surface can be prepared by peeling away older surfaces.

Liquid cells for the STM allow operation with the tip and the sample fully submerged in liquid, providing the capability for imaging hydrated samples. A liquid environment is useful for a variety of STM applications, including studies of biology, geologic systems, corrosion, or any surface study where a solid-liquid interface is involved. Like UHV, electrochemical cells provide a controlled environment for STM operation. Usually provided as an option for ambient STM, electrochemical-STM (EC-STM) consists of a cell, a potentiostat. Applications of EC-STM include real-space imaging of electronic and structural properties of electrodes, including changes induced by chemical and electrochemical processes, phase formation, adsorption, and corrosion as well as deposition of organic and biological molecules in electrolytic solution.

2.2.2 Tunneling Current

The calculation of the tunneling current (I_t) in an STM experiment is an important issue of the physics of STM, which is a complicated quantum mechanical problem involving the solution of Schrödinger equation in three dimensions and the modeling of the shape of the STM tip which, in most cases, is composed of an irregular and uncontrollable arrangement of atoms at its apex. It is nevertheless possible to simplify the problem with a series of reasonable approximations and reach a simple formula for the

tunneling current. The first approximation is to treat the problem using the first-order time-dependent perturbation theory [44-47] neglecting inelastic tunneling events:

$$I(V) = \frac{2\pi e}{\hbar} \sum_{\mu,\nu} \{f(E_\mu)[1 - f(E_\nu - eV)] - f(E_\nu)[1 - f(E_\mu - eV)]\} \mid M_{\mu\nu} \mid^2 \delta(E_\nu - E_\mu) \tag{2.20}$$

Where *f(E)* in the Fermi distribution, V is the applied voltage and $M_{\mu\nu}$ is the tunneling matrix element between quantum states and, respectively, of the tip and of the sample. An analytical expression for $M_{\mu\nu}$ was derived by Bardeen [48]:

$$M_{\mu\nu} = -\frac{\hbar^2}{2m} \int dS \cdot (\psi_\mu^* \nabla \psi_\nu - \psi_\nu \nabla \psi_\mu^*) \tag{2.21}$$

A simpler formula for the tunneling current requires the introduction of a few extra approximations, which apply to most of samples and tips used for STM experiments: (a) $M_{\mu\nu}$ is only a function of the energy U and tip-sample distance z, (b) $T = 0$ so that the Fermi distribution has a simple step-like shape, (c) we assume that the tip is very sharp so that the tunneling events are localized in space, (d) we ignore the effect of spin (not applicable for STM on magnetic materials). Given those approximations, the current can be written as a simple convolution of the (local) density of states of the tip and of the sample multiplied by a factor *M(U, z)*:

$$I(V,z) = \frac{4\pi e}{\hbar} \int_0^{eV} dU \rho_T(E_{F,1} - eV + U) \rho_S(E_{F,2} + U) M(U,z) \tag{2.22}$$

where $F_{F,1}$ and $F_{F,2}$ are the Fermi energies of the tip and sample. The local density of states (LDOS) can be written as:

$$\rho(r,E) = \sum_k |\psi_k(r)|^2 \cdot \delta(E_k - E) \tag{2.23}$$

this is a generalization of the usual expression for the density of states that takes into account the spatial modulation of the wave function. In the case of small voltage bias, the matrix element can be written (using the WKB approximation) as $M(k, z) = M_0 \exp(-2kz)$. A simple expression for k can be derived in the case of a rectangular barrier of height ΔW: $k^2 = 4\pi m(\Delta W + U) / h^2$. Furthermore, the density of states of the tip can be approximated as a constant for metal tips. With these additional approximations we obtain the following simplified expression for the tunneling current:

$$I_T(V,z) \propto e^{-kz} \int_0^{eV} dU \rho_S(E_F + U) \tag{2.24}$$

The physical interpretation of this formula is that (a) the STM current I_T 'measures' the local density of states of the sample and (b) that I_T varies exponentially with the tip-sample distance. An intuitive picture of the STM tunneling processes is to consider the current as being entirely emitted from the last atom of the tip and going directly into the sample beneath it at a distance z determined directly by the magnitude of the tunnel current.

A few more details have often to be taken into account to interpret the STM measurements. The most common ones are: tip convolution, double tip, and drift. The first two effects stem from the fact that a real tip is most likely not point-like in shape, as assumed in our simplified equations for the tunneling current. The image will thus be the result of a convolution of the tip-shape and the actual image of the sample. This

phenomenon can be best understood with an *experiment* of 'reversed STM', where the sample presents a very sharp (atomic) feature, while the tip is very blunt (e.g. has a diameter of a few tens of nanometers). In this case the role of the sample and the tip in the STM experiment are reversed and scanning one over the other produces an image of the tip taken by the protrusion on the sample. Any other topography taken with that particular tip will be convoluted with such an image which can therefore be considered as the 'signature' of the tip. Note that, knowing the STM imaging of the tip, it is possible to calculate back the real topography of the sample.

A 'double tip' is a particular case of tip convolution, where the tip has two sharp protuberances at the apex and thus all the sample features appear with a shadow-like replica.

Drift is another common cause of distortion of STM images: it appears as a continuous shift of the images towards one particular direction of the scan field. There are two main types of drift: thermal and electronic. The former is seen when the STM is not uniformly thermalized and, consequently, thermal expansion/contraction can cause the relative position of the tip and sample to change in time. This is normally seen in the topography as a constant drift of the image toward a fixed direction in space. Electronic drift has the same effect of thermal drift and can be caused by a variable offset in the high-voltage amplifiers that drive the scanner which is made of piezoelectric material. This effect is normally not observed in our STM control electronics. Another effect that gives distortions similar to electronic drift is 'piezoelectric creep': after a fast voltage

change the scanner will have a slow creep in time according to the formula $\Delta l/l = a + b \times \ln(t)$, where a and b are constants and t is the time.

2.2.3 Nanotube and Nanorod STM Probes

Carbon nanotubes and W based nanorods are very good choices for STM probes because their extremely small thickness and perfectly straight shape. In addition, they also have good electrical, mechanical, and chemical properties which are suitable for STM probe application. Both types of materials are good conductors, and they have high Young's (elastic) modulus (hard to be compressed). They are also very stiff so that the lateral mechanical vibration can be largely reduced. Chemically, CNT and WC nanorod cannot be easily oxidized, which is very useful for STM imaging in air. In addition, CNT has no solid oxide and WC is a high-hardness material. Therefore, they are also good for long-term STM operation.

Despite their excellent properties, it is still a difficult task to fabricate nanotubes and nanorods on the apexes of STM tips in a controllable way. First, their length must be controlled. Ideally, the nanotube on STM tip should be less than 500 nm to prevent the lateral vibration from significantly affecting the lateral resolution of the STM imaging. On the other hand, the length cannot be too short in order to image on rough surfaces (e.g. surface with steps). Second, the number of nanotubes or nanorods on the tip apex has to be limited. Obviously, too many nanotubes or nanorods on the tip apex will create difficulties for STM imaging. However, it is extremely difficult to ideally grow just one nanotube or nanorod on the tip apex while growing multiple nanotube or nanorods on the

tip apex is much easier. Therefore, synthesizing only a limited number of nanotubes or nanorods on the tip apex will be a more feasible way to fabricate the functional STM probes by considering that one of the CNTs or nanorods is usually longer than the others so that multi-tip problem may not arise. Finally, CNTs and nanorods are synthesized at high temperatures in various gas ambients, and their surfaces could be bonded with some chemical groups which might affect the performance of the STM probe. Therefore, in order to improve the probe's performance, post-treatment may be needed to recondition the CNT or nanorod surface.

CHAPTER III

EXPERIMENTS

In this chapter, the synthesis of CNTs and their applications in FEAs will be first introduced, and then the synthesis of W based nanorods and their applications in FEAs and STM probes will be presented. All technical details of the experiments will be provided, such as experimental setups, processing procedures and conditions, as well as characterization methods of materials and devices. The experimental results and the discussion of the results will be presented in the next chapter.

The nanomaterial synthesis techniques used in this dissertation work include microwave plasma CVD (MPCVD), thermal CVD, and thermal annealing. CNTs and W based nanorods are synthesized on various substrates based on the requirements of different applications. The structure of FEAs is fabricated in Si substrates using surface micromachining techniques. Nanorods are directly grown on electrochemically etched W tips to fabricate STM probes. The material and device characterization methods include Raman spectroscopy, SEM, TEM, STM and field emission measurements.

3.1 Synthesis of Carbon Nanotubes

The synthesis of carbon nanotubes has been realized and investigated using two types of CVD techniques: microwave plasma CVD and normal pressure thermal CVD. Since it is more difficult to grow CNTs on silicon (especially inside the silicon cavity) with microwave plasma CVD, only thermal CVD process is employed to fabricate CNT FEAs and CNT STM tips. In addition, thermal CVD process is more compatible with the

device manufacturing process. Both synthesis and characterization of CNTs have been conducted in this work.

The synthesis of CNTs is composed of three steps which include substrate preparation, catalyst application and chemical vapor deposition. Each process step as well as CNT characterization techniques will be described in the following sections.

3.1.1 Substrate Preparation

Three types of materials have been used as the substrates in the CVD synthesis of CNTs, which include silicon wafer, silicon dioxide and tungsten wire. Silicon wafer is suitable for surface micromachining to fabricate CNT FEAs. Tungsten wire is one of the standard materials for STM probes because of its rigidity, stable chemical properties and ease of fabrication of tungsten tips by electrochemical etching.

To prepare the substrates for CNT synthesis, silicon wafers are first sliced into small chips, then cleaned with acid solutions and deionized water. If oxide substrate is used, silicon chips need to be oxidized in high temperature furnace. Tungsten wire is electrochemically etched in KOH solution to make tips which can also be used as substrates for CNT synthesis. The details of substrate preparation will be described in device fabrication sections.

3.1.2 Application of Catalyst

Metal catalysts are generally needed for synthesis of CNTs using CVD process on silicon or silicon dioxide substrates. Nickel-chromium alloy in the form of thin film of about 10- nanometer thick is deposited on substrates as catalysts using RF sputtering.

3.1.3 CVD Synthesis of CNTs

Microwave CVD and thermal CVD are two of the most used CVD techniques for CNT synthesis. Both methods have been investigated with various process conditions in this dissertation study.

3.1.3.1 Microwave Plasma CVD

The experimental setup for microwave CVD is shown in Fig. 3.1. The vacuum chamber and vacuum pumps are used to provide low gas pressure for gas discharge which is created by the microwave that is generated in the microwave generator and coupled into the chamber through the waveguide and coupler. The sample is placed on a graphite stage which is heated by an inductive coil. The gas pressure and heater temperature can all be manually set and automatically maintained by two controllers. Microwave output power for the generator is manually adjustable. The position of sample holder (graphite stage) can be adjusted to change impedance of the vacuum chamber, the shape of the plasma ball and its contact with the sample. The two tuners on the waveguide are employed to achieve impedance matching that assures most of the microwave power can be coupled into the chamber. Gas mixture of H_2 and CH_4 is fed into the chamber for CNT synthesis. The gas flows are regulated by mass flow controllers. There are two viewports on the chamber wall, through which the sample is viewable and certain spectroscopic experiments can be carried out.

The processing steps for CNT synthesis is as follows. First, substrates with catalyst coatings are placed on the graphite heater stage and the vacuum chamber is pumped down below 10^{-4} Torr. Then the sample heater is turned on. When the heater temperature reaches the setpoint, hydrogen is introduced into the chamber and the sample holder/heater is raised up to an appropriate height. Finally, after the gas pressure gets to

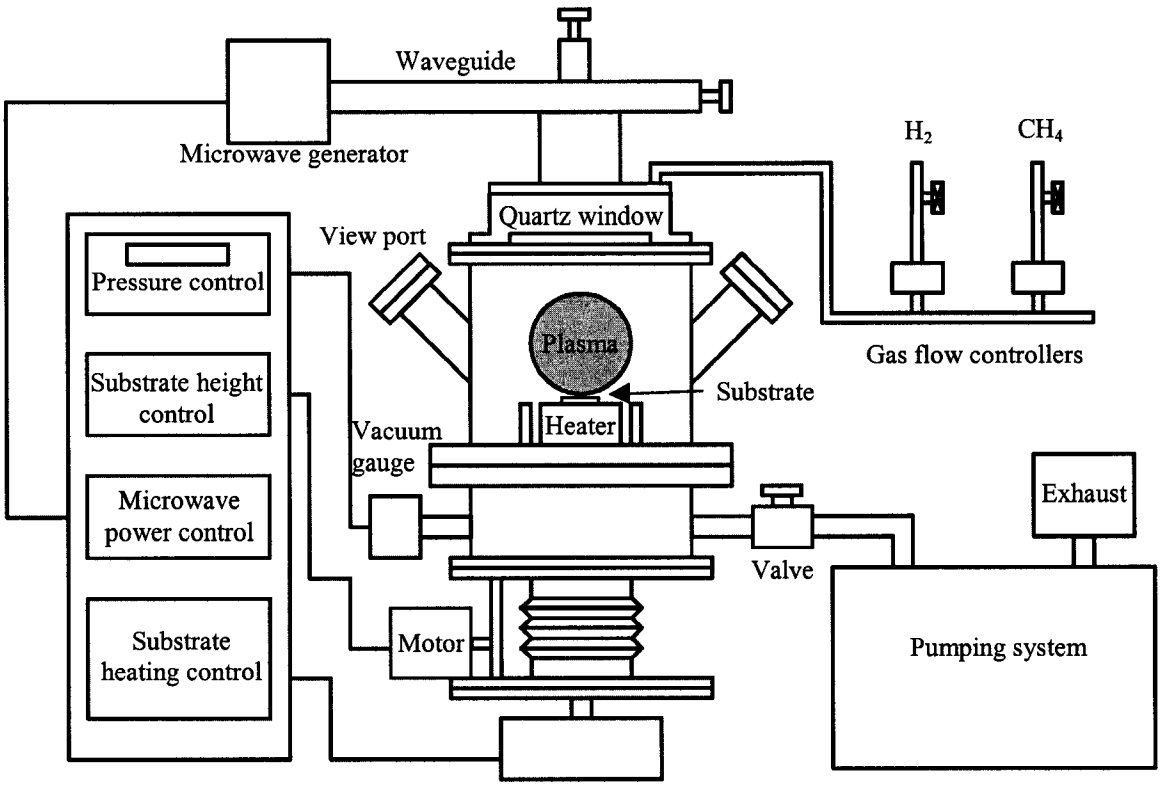

Fig. 3.1 Microwave plasma enhanced CVD system.

12 Torr, the microwave generator is switched on to start the plasma and the chamber pressure goes up to 30 Torr shortly after the creation of hydrogen plasma. CH_4 is fed into the chamber to start the CVD synthesis of CNTs. After a few minutes, the CVD process is stopped by shutting down CH_4 and plasma generator. The sample is cooled down in H_2 flow without heating. It should be noted that the starting of the plasma and the CVD process are performed at two different chamber pressures. It is because hydrogen plasma can only be started at a gas pressure below 20 Torr depending on the heater temperature. Another reason is that plasma heating is stronger at higher pressures, which is helpful for enhancing the CVD process. The process conditions for CNT synthesis by microwave CVD are listed in Table 3.1.

Table 3.1 Experimental conditions for CNT synthesis by microwave CVD

Base pressure	$< 10^{-4}$ Torr
Heater temperature	600-800 °C
Gas pressure	30 Torr
Microwave power	800-1000 W
H_2 flow rate	300-450 sccm
CH_4 flow rate	1%-30% of H_2 flow rate
Sample holder height	58 mm

3.1.3.2 Normal Pressure Thermal CVD

Normal pressure (atmospheric pressure) thermal CVD is another useful CVD technique for CNT synthesis, which utilizes the catalytic thermal decomposition of

hydrocarbon gases and is much simpler to implement compared to microwave CVD. In addition, thermal CVD is also more suitable for device applications. Like the CNT FEA and CNT STM tip studied in this work, microwave CVD has been applied to grow CNTs for those devices. However, CNTs grown on small, discrete catalyst islands will be quickly etched by hydrogen plasma, thus making it difficult to grow CNTs on silicon. Therefore, the experimental results are inconsistent.

The experimental setup for normal pressure thermal CVD is just like a miniaturized and simplified high-temperature quartz tube furnace compared with a standard system. It has only one heating zone and one thermo couple for temperature measurement while a standard tube furnace generally has three heating zones for extended length of the constant temperature zone (flat zone). Since the thermal CVD process is conducted in the quartz tube at atmospheric pressure, there is no need for a vacuum pump. All the tubing connections are air-tight in order to avoid air leaking into the quartz tube. Gas flow rates are regulated by mass flow controllers and the furnace temperature is manually set by adjusting the voltage applied on the electric heater.

The experimental steps for CNT synthesis by normal pressure thermal CVD are as follows. Place the sample into the quartz tube and push it to the center of the furnace. Flush the system for 5 min with H_2 gas flow (500 sccm) to expel the air out of the quartz tube and gas line. Turn on the heater and let the sample being heated and baked in H_2. When the furnace temperature reaches the process temperature, reduce H_2 flow rate and open the valve for C_2H_2 to start the CVD process. C_2H_2 can also be fed in the system as gas burst lasting for a few seconds. After the CVD process is finished, the sample cools down in H_2 flow. Although the thermal CVD process can also be performed in other gas

mixtures using C_2H_4 and carrier gases like Ar and Ammonia, the samples are always heated up in H_2 ambient prior to the CVD reaction. The experimental conditions for CNT synthesis by normal pressure thermal CVD are listed in Table 3.2.

Table 3.2 Experimental conditions for CNT synthesis by thermal CVD

Furnace temperature	600-800 °C
Carrier gases	H_2, Ar, Ammonia
Flow rate of carrier gas	50-100 sccm
Hydrocarbon gases	C_2H_2, C_2H_4
Flow rate of hydrocarbon gas	< 10% of carrier gas

3.1.4 Characterization

The synthesized CNTs can be characterized by several analytic techniques. SEM is employed to provide the morphological information about CNTs, like their length, diameter, orientation, straightness, number density, and some information of the catalytic metal particles. TEM can be used to accurately measure the tube diameter and clearly display the atomic layer stacked structure of the tube wall on high-resolution TEM images which are also useful for estimating the quality of CNTs. Any defects or metal particles encapsulated in CNTs can be found out on TEM images. Raman spectroscopy is an analytic technique which can effectively analyze the composition of materials. It is actually a standard method to determine the contents of different carbon structures in a material. Therefore, it can be used to measure the content of non-graphite carbon deposited with CNTs. Field emission properties of CNTs are also studied considering

CNT is a promising cathode material for field emission applications. The field emission tests are conducted using diode configuration.

3.2 Fabrication of CNT Field Emitter Arrays

Fabrication of CNT FEAs is composed of many processing steps which will be described in the order that they are performed. The whole process of CNT FEA fabrication is illustrated in Fig. 3.2.

3.2.1 Substrate Preparation and Cleaning

The specifications of the n-type silicon wafers used for CNT-FEA fabrication are 2-inch <100>-orientation, phosphorus doped and resistivity of 1-10 Ω·cm. Each wafer is first sliced into 8 mm × 8 mm square chips with a SiC scriber. The cutting lines (4 sides of the square chip) are along the <110> directions. These small chips are then soaked in acetone with ultrasonic agitation to dissolve organic contaminants and remove the debris produced during wafer scribing. After cleaning in acetone, the chips are boiled in a 95:5 mixture of concentrate sulfuric acid (98 wt.%) and hydrogen peroxide (30 wt.%) at about 120 °C with ultrasonic agitation to remove the remaining metallic and organic contaminants. The cleaning solution has a strong oxidizing effect that can form a thin layer of oxide on the surface making it hydrophilic. The oxide layer is subsequently removed by dipping the chip in diluted hydrofluoric acid (2.5 wt.%). In the end, all the chips are rinsed in deionized water and blown dry with hot air. This cleaning process is applied to all samples prior to the thermal oxidation.

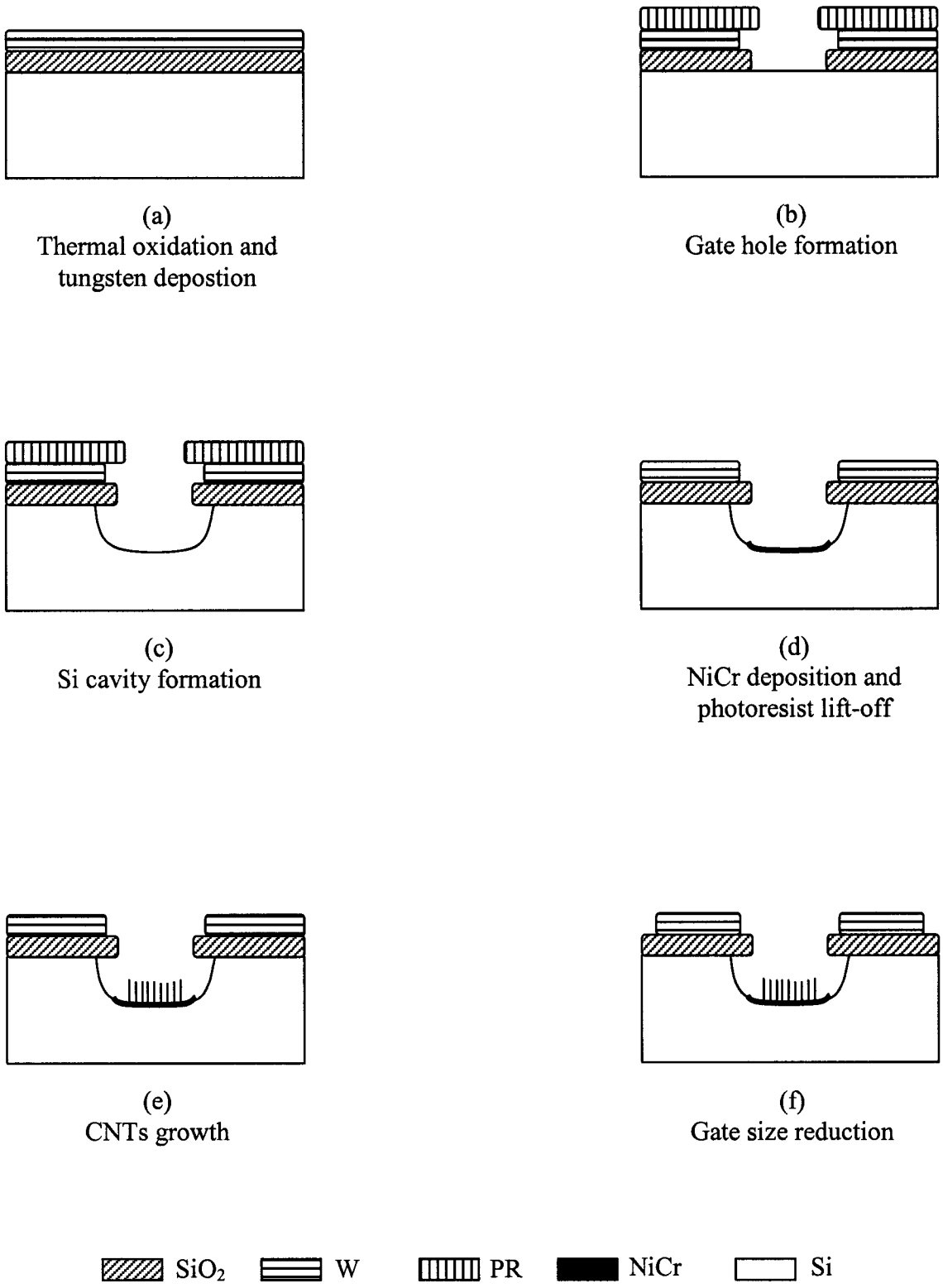

Fig. 3.2 Process flow chart for fabrication of CNTs based FEAs.

3.2.2 Thermal Oxidation

Immediately after the chips are cleaned, they are placed onto a flat quartz boat for thermal oxidation. Although dry oxidation, in which only oxygen is used, produces higher quality silicon dioxide, its oxidation rate is much lower than wet oxidation that uses water vapor as the oxidizer. The chemical equations that govern the dry and wet oxidations are given below.

$Si + O_2 \rightarrow SiO_2$ (dry oxidation)

$Si + 2H_2O \rightarrow SiO_2 + 2H_2\uparrow$ (wet oxidation)

For a given length of time, wet oxidation can create a much thicker oxide which can withstand a much higher breakdown voltage that that of oxide formed in dry oxidation. It is the reason why wet oxidation is chosen to prepare the oxide (insulator) between the gate metal and the Si substrate (cathode).

A three-zone high temperature tube furnace (Lindberg) is used to perform the silicon oxidation. A high-purity nitrogen gas (Research Grade, 99.995%) is fed through a flow-meter into a hot water bubbler, in which water is heated to 90-95 °C. When nitrogen comes out of the bubbler and enters the furnace tube, it also carries a lot of water vapor that can largely enhance the oxidation rate.

The temperature of the furnace is set at 1050 °C for the center zone, both end zones' temperatures are set 15% higher than the center zone's set-point for a flat temperature profile along the quartz tube. The silicon chips sitting on the quartz boat are transported and kept in the flat temperature zone during the oxidation process for the purpose of minimizing the chip-to-chip variation of the oxide thickness.

All samples are oxidized under the same conditions which are summarized in Table 3.3 When the samples are transported into or out of the quartz tube, a slow one-minute push-in or pull-out is performed to avoid excessive thermal stress induced by the rapid temperature change associated with the fast sample movement.

Table 3.3 Experimental conditions for wet thermal oxidation of silicon

Furnace temperature (center zone)	1050 °C
Gases	$N_2 + H_2O$
Nitrogen flow rate	0.2 lpm
Water temperature	90 – 95 °C
Push-in/pull-out time	1 min
Oxidation time	1 hr
Oxide thickness	0.4 μm

An oxide breakdown test is carried out to evaluate the oxide quality. The measured breakdown voltage is volts, or in term of electric field V/μm. Although the measured breakdown field is lower than the commonly referenced value of 10^3 V/μm, the oxide quality is still good enough for use as the insulating layer between the gate and the substrate. The impurities introduced during the cleaning and oxidation process are believed to be the major factors that attribute to the degradation of oxide quality.

3.2.3 RF-sputtering of Tungsten

The metal gate is a thin film of pure tungsten that is deposited on top of the oxide in an RF-sputtering system (Cook Vacuum). The choice of tungsten as the gate material is

based on its high melting point, good adhesion to silicon dioxide and ease etching during the gate patterning. As a result, the tungsten gate can withstand the high temperature during the CNT growth process, and the gate film will not peel off from the sample surface.

Immediately after thermal oxidation, the sample will be moved into the vacuum chamber without long-time contact with the air, which may degrade the adhesion between the tungsten film and the oxide because of the accumulation of moisture and micro-dusts on the oxide surface. The sputtering conditions for tungsten film deposition are listed in Table 3.4.

Table 3.4 RF sputtering conditions for gate metal deposition

Target material	Tungsten
Base vacuum	$< 3\times10^{-6}$ Torr
Working pressure	70/10 mTorr (2 gauges)
RF power	110 W
RF voltage	1800-1900 V
Gas	Argon (UPC grade)
Time	20 min

The deposited film is about 0.2 μm thick, and its sheet resistance is 0.3 Ω/ that is measured by 4-point probe test. The sheet resistance is low enough to avoid significant voltage variation along the gate metal layer through which a normal gate current, < 1 mA,

flows to the contact point where the gate voltage is applied from external circuit. The sketch of cross-sectional view of the device after tungsten deposition is shown in Fig. 3.1(a).

3.1.4 Photolithography and Wet Etching for Gate Hole Formation

Photolithography and wet etching are used to make arrays of gate holes through the gate metal layer and the oxide. The pattern of the photomask used for the photolithography is an 200×200 array of 5 μm-in-dia. circular holes that are arranged with a center-to-center separation of 20 μm in the center of an 8×8 mm^2 metal film which is opaque to UV.

Positive photoresist (Shipley Microposit 1813) is used for all photolithography processes and the UV exposure for pattern transfer is performed on a MJB 3 UV300 mask aligner (Karlsuss) in contact mode. The photolithography process includes photoresist spin coating, pre-bake (soft bake), UV exposure, post-exposure bake (optional), photoresist development, and post bake (hard bake). The process conditions for photolithography are listed in Table 4.3. The photoresist thickness is a nominal value. All bakes are done on a hotplate with the same temperature. The photoresist is developed in Microposit 352 developer (Shipley) at room temperature that is ~19 °C in our clean room where all wet processing is conducted and all chemicals are stored.

When photolithography process is completed, the pattern is transferred from photomask to photoresist layer. The 200×200 array of round holes have been formed through the photoresist layer. These holes act just like windows where the underlying tungsten film is exposed. Therefore, selective etching of tungsten film can be performed via these windows.

Table 3.5 Processing conditions of photolithography for gate hole formation

Spin speed	4500 rpm
Pre-bake termperature	105 °C
Pre-bake time	1 min
Photoresist thickness after pre-bake	1.6 μm
UV intensity	27 mW/cm^2
Exposure time (contact mode)	12 sec
Post-exposure bake time	1 min
Developing time	20 sec
Post-bake time	2 min

Tungsten etching is conducted in a 30% H_2O_2 solution (J. T. Baker, VLSI grade) at about 19 °C. Obviously, the time needed for etching through the tungsten film depends on the thickness of tungsten film, air temperature, and the concentration of H_2O_2 solution. Occasionally, the etching time varies significantly from batch to batch. In order to avoid over-etching or under-etching, one sample is always picked out from each batch to be used as a "dummy" that is etched before other samples to determine the appropriate etching time. The time for tungsten etching usually is about 3 min.

When tungsten etching is finished, selective etching on the oxide layer can be carried out through the holes formed during tungsten etching. The standard oxide etching solution (J. T. Baker, 5:1 Buffered Oxide Etch) is used to etch the thermally grown SiO_2. The etching process can be described by the following chemical equation

$$SiO_2 + 4HF \rightarrow SiF_4 + 2H_2O$$

The etching rate is about 0.1 μm/min at room temperature, and the solution does not etch tungsten, silicon, or photoresist.

After photolithography and wet etching process, the cross-section view of the FEA sample is illustrated in Fig. 3.1(b). Now, the gate hole is complete, and the next step will be silicon etching for cavity formation.

3.2.5 Dry Etching of Silicon – Cavity Formation

The cavity in silicon is created to accommodate vertically aligned carbon nanotubes. The silicon cavities can be made by selective etching through the gate holes. The silicon etching process can be either wet etching or dry etching. The etching starts from the silicon surface exposed in the gate holes, and the cross-section view of the etched profile (cavity) may have different shapes depending on the etching process used. In this dissertation research, plasma etching is applied to create the silicon cavity.

Plasma etching is a commonly used dry etch technique, and the etching systems have many different configurations, which are related to different etching processes and properties. For instance, the plasma etching system (PlasmaTherm) used in this study can operate in either the plasma etch mode or reactive ion etch mode. The plasma etching system is composed of two parallel-plate electrodes. For plasma etch mode, the upper electrode is powered by RF generator while the lower electrode and the chamber wall are grounded. The samples are placed on the lower electrode. This configuration makes the etching system operate in plasma etch mode that has a higher working pressure and a lower sheath field than those of reactive ion etch (RIE) mode in which the lower electrode is powered by RF source while the upper electrode and chamber wall are

grounded. When the etching system runs in RIE mode at low working pressure and high sheath voltage, it results in more anisotropic etching due to the enhanced directionality of ion bombardment and increased ion bombardment energy. Therefore, lateral etching is minimized in RIE mode, and RIE is not suitable for making silicon cavity. On the contrary, etching rate in plasma etch mode is isotopic in all directions, leading to an undercut etching under the oxide mask. Therefore, metal catalyst will not be deposited on the side wall of the cavity to create a shorting path between the gate and the cathode.

3.2.6 Wet Etching of Tungsten – Overhanging Gate Removal

During the process of gate-hole formation, the oxide is over-etched in order to avoid deposition of catalyst on oxide. Therefore, part of the gate metal is overhanging without the support from the oxide, which could be a reliability problem. On the other hand, some of the electrons, which are emitted from CNTs grown in the cavity, definitely will be collected by the overhanging gate when they are moving out of the cavity through the gate-hole.

The overhanging part of the gate metal is removed by wet etching that is the same etching process used in gate-hole formation. The etching starts from the inner side of the tungsten film because the outer side is covered by photoresist. Since the etching starts from the inner side, the small gate-hole and longer diffusion path can limit the species exchange, which leads to a lower etching rate. So 5-minute is needed for completely etching off overhanging tungsten in stead of 3-minute used in the gate-hole formation step.

3.2.7 RF Sputtering of NiCr -- Catalyst Deposition

Catalyst is required for synthesis of CNTs using CVD process. In this dissertation research, a nickel chromium alloy (NiCr: 80% Ni + 20% Cr) is used as the catalyst for decomposition of hydrocarbon gases. NiCr is deposited into the silicon cavity by using RF sputtering that has the same processing conditions as described in the gate metal deposition except different sputtering time; a sputtering time of only 1-minute for NiCr is used.

3.2.8 Photoresist Removal and NiCr Lift-off

When NiCr deposited into the silicon cavity, NiCr is also deposited on top of the photoresit. Since photoresist and NiCr on it are no longer need for the next processing steps, both of them need to be removed. Their removal can be easily conducted by immersing sample in acetone which readily dissolves the photoresist through the pinholes and gaps on the very thin NiCr film. Meanwhile, NiCr thin film gets lifted off with the photoresist being dissolved in acetone. Finally, the samples are rinsed with ethanol and de-ionized water to get rid of any metal debris remaining on the sample.

3.2.9 Gate Metal Downsizing

Along the edges of the FEA chip, the gate metal is separated from the Si substrate with a thin layer of insulator (silicon dioxide) in between which will be damaged or contaminated during the whole fabrication process, resulting in a large leak current or even a breakdown (shorting) when an electrical voltage applied across the gate and the substrate. To avoid this problem, one more photolithography and wet etching process is applied to reduce the size of the tungsten gate. This step is conducted with the same conditions as the process that makes the gate hole through the tungsten thin film.

3.2.10 CNT Synthesis - Thermal CVD

This is the last step to make CNT FEA. It is performed in the same way as described in Section 3.1.3.2. CNTs will be only grown inside the silicon cavity at the bottom while no CNTs or any carbon will be deposited on the metal gate, the oxide and the sidewall of the cavity.

3.2.11 Characterization of CNT FEAs

The performance of CNT FEAs is evaluated with field emission tests. The CNT FEA chip is mounted on a TO-10 header with silver epoxy. The gate is connected to one of the pins through a thin copper wire. A small piece of copper foil is used as the anode with a separation of several millimeters to the FEA chip. All these devices are connected and mounted on a vacuum electrical feed-through which provides the connections to the power sources and instruments outside the vacuum chamber. The vacuum status inside the vacuum chamber is monitored with an ionization gauge.

3.3 Synthesis of Tungsten Oxide Nanorods

Tungsten trioxide nanorods are synthesized using thermal annealing at atmospheric pressure, which is very similar to the thermal CVD method described in Section 3.1.3.2 used for synthesis of CNTs. However, unlike the synthesis of CNTs, no catalyst is used for nanorod growth.

3.3.1 Substrate Preparation

In the experiments, various W substrates are used, including W wires (0.25 mm diameter), electrochemically etched (in 2M KOH solution) W tips, W foils (0.25 mm thick), and RF sputtered W films (50 nm thick). The tungsten wires and foils are cleaned in acetone and deionized water prior to thermal annealing to remove any grease and dust particles on the surface. Electrochemically etched W tips are prepared in the same way as

described in Section 3.3.1. RF sputtered W films are deposited on Si substrates using the same process presented in Section 3.2.3 except that a shorter deposition time of 5 min is used instead of 20 min because 50 nm thick W film is sufficient for nanorod growth.

3.3.2 Thermal Annealing

Tungsten substrates are annealed at atmospheric pressure in a quartz tube furnace (13 mm inner diameter) using a resistive heater, which is the same as the experimental setup introduced in Section 3.1.3.2. The quartz tube and the gas lines are first purged for a few minutes with high-purity hydrogen of a high flow rate of 1000 sccm, and then the samples were heated at an average temperature ramp-up rate of about 150 °C per minute. When the temperature was 100 °C below the annealing temperature, the hydrogen flow was reduced to 200 sccm. As the furnace temperature reached the annealing temperature, hydrogen was cut off followed by an Ar flow of 100 sccm. After the samples were annealed in argon for 2-10 minutes, samples were cooled down in argon flow. Annealing temperatures ranging from 650 °C to 900 °C were used in the experiments.

3.3.3 Characterization

The nanorods produced by thermal annealing are investigated using various analysis methods including SEM, HRTEM, selected area diffraction (SAD), and EDXS which provide useful information about the structures and composition of the nanorods.

3.4 Fabrication of Nanorod Based Field Emitter Arrays

Nanorod based FEAs are fabricated on n-Si (100) substrates using the surface micromachining techniques. The processing steps for the fabrication of nanorod based FEAs are very similar to the fabrication of CNT FEAs (See Fig. 3.2) except that the dry etching of Si to form the cavity is not needed any more and W instead of NiCr is

deposited in the cavity for W nanorod synthesis. Since the growth of W nanorods is not so fast as that of CNTs, the length of W nanorods can be readily controlled within certain range so that the Si cavity is unnecessary to accommodate long nanorods. Whether W nanorods or WC nanorods synthesized in FEAs depends on the gases used in the last step of nanorod synthesis.

The nanorod FEAs are tested in the same way as CNT FEAs are tested, which is presented in Section 3.2.11.

3.5 Fabrication of Nanorod STM Probes

The fabrication of W based nanorod STM probes is composed of three steps: the making of tungsten tips, tip surface treatment, and synthesis of W based nanorods on tungsten tips.

3.5.1 Making of Tungsten Tips

Tungsten tips are made using electrochemical etching in aqueous solution of potassium hydroxide (KOH). The tungsten wire used to make the tips has a purity of 99.95% (metal basis) and it is 0.25 mm in diameter. The molarity of the KOH solution in the container is 2 M. Tungsten wire is immersed in KOH solution 3-4 mm below the liquid surface.

Tungsten tips can be made with DC or AC etching. The DC etching (anodic etching) is performed in such a way that the tungsten wire (anode) placed in the middle of the silver loop (cathode) which is half immersed in the solution with the loop plane aligned with the liquid surface. Tungsten wire is connected to the positive output terminal of the DC power source while the silver loop (cathode) is connected to the negative terminal. A DC voltage of 13 V is applied across the anode and cathode during the electrochemical

etching. The electrochemical reactions occurring on the anode and the cathode can be characterized by the chemical equations given below.

Anode: $6H_2O + 6e^- \rightarrow 3H_2$ (gas) $+ 6OH^-$

Cathode: W (solid) $+ 8OH^- \rightarrow WO^2_4 + 4H_2O + 6e^-$

W (solid) $+ 2OH^- + 2H_2O \rightarrow WO^2_4 + 3H_2$ (gas)

3.5.2 Selective Surface Treatment to Tip Apex

In order to enhance nanorod growth on the very top of W tips, a dedicated process of surface abrasion in diamond slurry (suspension of diamond nanoparticles in water) is applied to only treat the tip apex while the other parts of tip surface are protected by a coating of photoresist. Photoresist coating on w tips can be conveniently implemented by dipping W tips 2-3 times into positive photoresist. And then the tips are baked in a desktop oven at 110 °C for 3 min. The photoresist coating can also be dried with a hot air blower.

Since the whole tip surface is covered by the photoresist coating, an opening needs be created to expose the tip apex for surface abrasion. A simple process has been developed to make the opening. Photoresist coated W tips are first placed in the small tubes fixed on a movable stage. The movable stage is driven by a threaded rod which can be rotated manually. By turning the threaded rod, the stage moves slowly toward a Si chip that is fixed on the right end of the setup. When W tip touches the Si chip, the stage stops moving and the left end of the setup is raised up to create a pressure onto the tip apex. The pressure is controlled by the tilted angle or the height of the left end of the setup. When the pressure is high enough, W tip can breach through the soft photoresist coating and an opening is created on the tip apex. Since the stage moves slowly and the

pressure applied on the tip apex can be controlled, the tip will not be bent. Furthermore, multiple tips can be processed at the same time.

After the photoresist on the tip apex is removed, the tips are immersed in diamond slurry with ultrasonic agitation for 30 sec. Then the photoresist is removed with acetone and rinsed with ethanol and de-ionized water. Finally, tungsten tips are treated in H_2O_2 or HF solution for 5 sec and ready for synthesis of nanorods via thermal annealing.

3.5.3 Synthesis of Nanorods on W Tips.

Tungsten tips are inserted into a small bundle of ceramic tubes with small holes and then are placed in the quartz tube and pushed to center of the furnace. The process conditions and procedures are the same as described in Section *3.3.2.*

3.5.4 Characterization of Nanorod STM Probes

Nanorod STM probes are observed using SEM. The length, thickness, and the number of nanorods grown on the tip apex can be clearly determined on SEM images. STM experiments with nanorod probes are performed to obtain atomic resolution images for evaluating their performance.

CHAPTER IV

RESULTS AND DISCUSSION OF CARBON NANOTUBES

In this chapter, the experimental results of CNTs will be presented and discussed in three sections. In the first section, the results of the synthesis and characterization of CNTs produced by MPCVD will be provided with detailed discussion. In the second section, the results of the synthesis and characterization of CNTs produced by thermal CVD will be presented and discussed. In the last section, results of CNT FEA fabrication and field emission tests will be introduced and discussed.

4.1 Synthesis and Characterization of CNTs Synthesized by MPCVD

In this section, the synthesis of CNTs will first be discussed followed by the characterization of morphological and structural properties of CNTs using SEM, TEM, and Raman spectroscopy. Subsequently, the electron field emission characteristics of the synthesized CNTs will be discussed.

4.1.1 Synthesis of CNTs by MPCVD

CNTs had been synthesized using MPCVD under various process conditions on SiO_2/Si substrates coated with NiCr film. First of all, various substrate heater temperatures within the range of 500 °C to 800 °C were tried in the MPCVD process. The CNT synthesis was successfully realized through the entire temperature range mentioned above. However, when the heater temperature was below 600 °C and approaching 500 °C, the amount of synthesized CNTs decreased significantly and the field emission performance was poorer compared to those of CNTs synthesized at higher temperatures. This is because lower temperatures limit the catalytic effect of NiCr film, and the

diffusion of carbon through the catalyst particles is also slowed down. On the other hand, when the heater temperature is above 700 °C, the etching of CNTs by hydrogen plasma will be enhanced so that synthesized CNTs will be damaged resulting in poor field emission. The etching of CNT is observed to start from the edge of the substrate. Therefore, this effect is even more severe when CNT growth is performed patterned NiCr film (an array of small NiCr squares which are 60 × 60 μm^2). The effect of etching CNTs by hydrogen plasma will be further discussed later in this section. In order to obtain good field emission results, CNT growth by MPCVD is generally conducted at 600 °C – 650 °C. However, the real temperature at the substrate surface could be considerably higher than the heater temperature because of the plasma heating.

The effect of methane flow rate was also investigated. MPCVD experiments demonstrate that a wide range of methane flow rates can be used for synthesis of CNTs except that a very low methane flow (e.g. 1% of hydrogen flow) will produce poor or no yield of CNT growth. As long as methane flow rate is larger than 5% of hydrogen flow, CNT synthesis can be readily achieved. However, higher methane flow rates (> 10% of hydrogen flow) do not show improved CNT yield when compared to those lower methane flow rates (e.g. 5% - 10% of hydrogen flow). On the contrary, they can only produce a much more deposition of non-nanotube carbon products on the substrate surface and chamber walls. Therefore, methane flow is generally set at 5% - 10% of hydrogen flow for synthesizing CNTs, and those CNTs performed the best in field emission tests.

In addition to methane, acetylene had also been successfully used in MPCVD as a hydro-carbon source which produces similar CNTs as methane does. However, since

acetylene decomposes much more readily and it has much higher C/H ratio than methane, more non-nanotube carbon products will be deposited on the substrate and chamber walls. To avoid possible contamination to other MPCVD processes from the excessive carbon deposited on the chamber walls, only methane was investigated for CNT synthesis using MPCVD.

CNT synthesis was also carried out under various gas pressures from 12 Torr to 60 Torr which is the pressure range that the MPCVD system can operate properly. Based on the observations during the MPCVD process and the observations on the synthesized CNTs, gas pressure has a rather similar effect as heater temperature. When gas pressure is higher, the plasma heating will be stronger making the substrate emit more intense visible and thermal radiation. Other than the plasma heating effect, no other effect on CNT synthesis was found by varying gas pressure.

MPCVD synthesis of CNTs was also performed on Si substrates coated with NiCr thin film. However, this only resulted in the deposition of non-nanotube carbon on sample surface, and no CNT growth was observed on Si substrates. Carbon deposition was first observed after the plasma was turned on, then the deposited carbon can be quickly removed by hydrogen plasma etching. This indicates that metal silicide is formed at elevated temperatures, and therefore no CNTs can be grown as metal silicide does not possess the catalytic effect for decomposing methane.

4.1.2 Characterization of CNTs Produced by MPCVD

SEM micrographs of CNTs synthesized by MPCVD with various growth times are shown in Fig. 4.1 Those are cross section views of cleaved CNT films grown for 2, 5, 10, and 30 minutes with a gas mixture of hydrogen and methane at flow rates of 300 and 30

sccm, respectively. Vertically aligned CNTs with a length of a few micrometers are densely packed to form a continuous film that is covered by nanoparticles which are NiCr particles coated with carbon. This clearly demonstrates that nanotubes are synthesized via head growth mechanism. The vertical alignment is produced by the self-biasing induced field (sheath field) near the sample surface as the sample surface contacts the plasma [49].

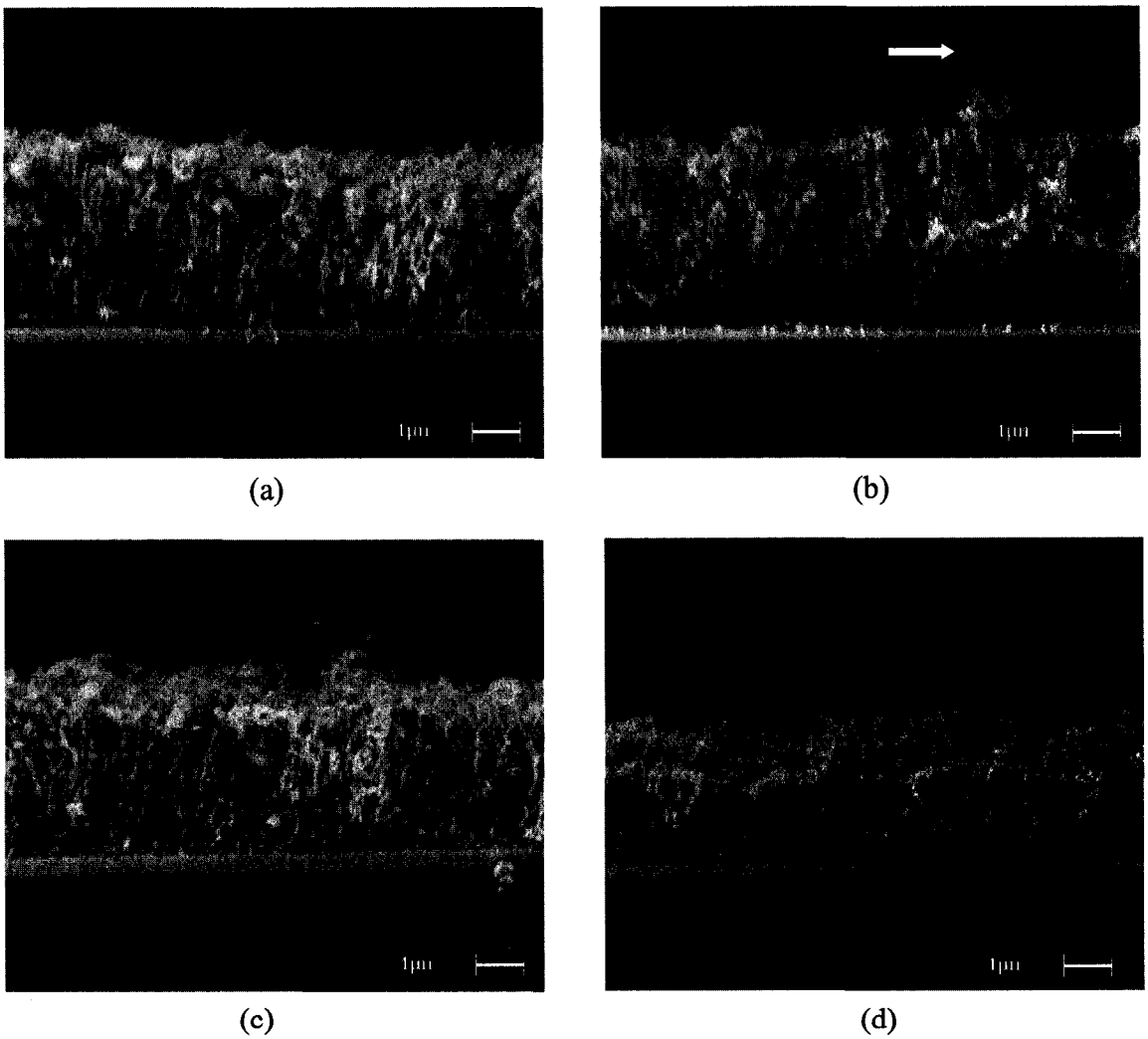

Fig. 4.1 SEM micrographs of CNTs grown by MPCVD with various growth times: (a) 2 min, (b) 5 min, (c) 10 min, and (d) 30 min. The scale bar size is 1 μm.

The effect of growth time on CNT film's morphology is not significant when the growth time is less than 10 minutes. All CNT samples exhibit similar film thickness as long as the growth time is not over 10 minutes. It seems that the thickness of CNT film quickly reaches its maximum of about 4 μm during the first a couple of minutes of growth, and it then remains constant and is independent of the growth time until 10 minutes. This phenomenon is also in agreement with the observation of the substrate surface during the MPCVD process, which turns black shortly (< 1 min) after the plasma is turned on. The termination of the growth of CNT film is due to the carbon coating on the catalyst particles, which prevents the gaseous hydro-carbon components decomposing and diffusing into the catalyst particles.

For samples grown for 30 minutes, a distinct decrease of the thickness of CNT film is observed from the SEM micrograph show in Fig. 4.1(d). Similar phenomenon has been reported by Choi et al. but short of a detailed explanation [50]. In fact, it was found that for samples grown for more than 10 minutes the CNT films were showing signs of etching starting from the corners and edges of the substrates with the corners being attacked more. Longer growth time results in more severe etching. This etching effect is due to the abundant atomic hydrogen existing in the plasma during the CNT growth. It is well known that atomic hydrogen is essential to the CVD synthesis of diamond where it is employed to remove amorphous carbon and graphite from diamond surfaces and bond with the surface carbon to sustain the diamond growth. Since the process conditions used for CNT growth are similar to those used for CVD diamond growth except the CH_4/H_2 flow rate ratio and the use of metal catalyst, it is reasonable that the reactive atomic

hydrogen would attack some weakly bonded carbon atoms or defected structures among the CNT film and thus causes the etching effect.

Another important observation can also be found in Fig. 4.1. Starting from 5-min growth, there are fine straight nanotubes (pointed by arrows) protruding from the CNT film surface, which are much longer, thinner and more straight than the other type of CNTs that form the CNT film covered by carbon coated catalyst particles. But they are also much fewer in number than the other type of CNTs. Unlike the bulk CNT film, these fine CNTs do not seem to be subject to the etching effect and keep growing with time as it can be seen in Fig. 4.1(c) and (d). As the thin CNTs grow longer, the rigidity of those CNTs may no longer be able to hold them straight, CNTs start bending as shown in Fig. 4.2(d). The above results clearly demonstrate the existence of two types of CNTs which exhibit very different morphological and chemical properties.

In order to further investigate the two types of CNTs, HRTEM analysis on the structures of CNTs was performed. CNTs synthesized on Si_2O/Si substrates were dispersed in alcohol with the assistance of ultrasonic agitation. CNTs can be readily detached from the substrate surface using this method, indicating a weak bonding between SiO_2 and CNTs. After CNTs were cleared off from the substrate surface, the oxide was fully exposed with almost all catalyst particles removed.

A low-magnification TEM image is shown in Fig. 4.2(a) in which both types of CNTs are included and specified as Type A and Type B. Those CNTs were grown for 10 min. Remarkable difference can be easily observed in the TEM image. Type A CNTs are multi-walled and their tube diameters are mostly larger than 20 nm. These CNTs contain various structural defects, which cause the irregular tube shape and diameter. Bamboo

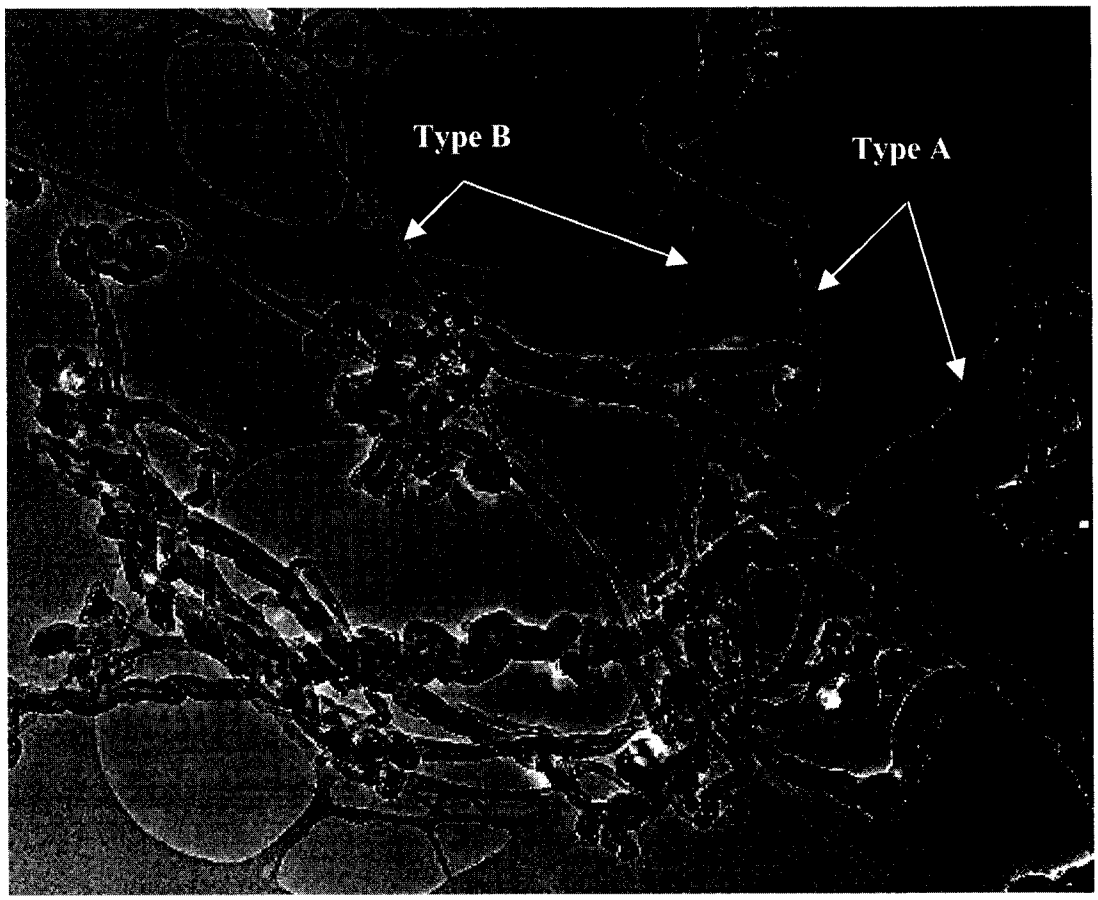

(a)

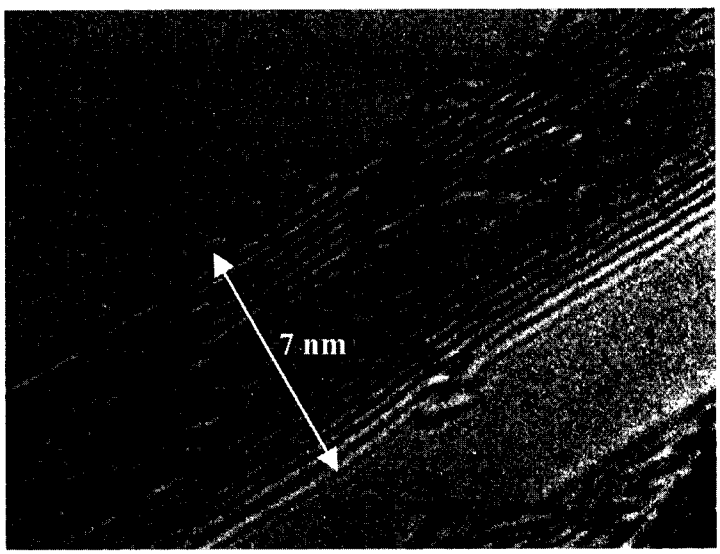

(b)

Fig. 4.2 HRTEM micrographs of CNTs produced by MPCVD using NiCr as catalyst: (a) low magnification image showing two types of CNTs; (b) high magnification image showing a well structured ultra-thin multi-walled CNT

type structure and catalyst particle filling, which are typical of CVD grown CNTs, are commonly observed among this type of CNTs. Type B CNTs, however, are totally different from Type A CNTs with thin and long straight tubes that are almost free of defects along the length direction. A high-magnification HRTEM image of a Type B CNT is shown in Fig. 4.2(b). The outer diameter of the CNT shown is measured to be 7 nm with a tube wall of seven graphene layers separated by a spacing of about 0.34 nm that is in agreement with the reported interlayer spacing for MWCNTs, which spans a range of 0.338 nm to 0.341 nm for MWCNTs of different chiralities. MWCNTs of such a small diameter have rarely been reported for MPCVD synthesis of CNTS. CNTs similar to Type B CNTs have been found among those grown by arc discharge [14], where the CNT growth conditions are completely different from those in MPCVD process. The perfect tube wall structure supposedly makes Type B CNTs much stronger as compared to Type A CNTs that can be etched by atomic hydrogen while Type B CNTs can withstand the attack.

The reason why two very different types of CNTs have been synthesized on the same substrate under the same process conditions is still unknown. Although catalyst particles are commonly observed encapsulated in Type A CNTs, metal particles have not been found in Type B CNTs. However, it has been confirmed that CNTs cannot be synthesized by using CVD method without metal catalysts. Our experimental results also verify this effect. Fig. 4.3 is a SEM micrograph showing a top view of CNTs grown on an array of NiCr squares. No CNT growth is found at regions where catalyst film had been removed. The result demonstrates that CNT growth is determined by the existence of

catalysts. Such effect can be applied to fabricate gated FEAs with CNTs only grown in the cavity.

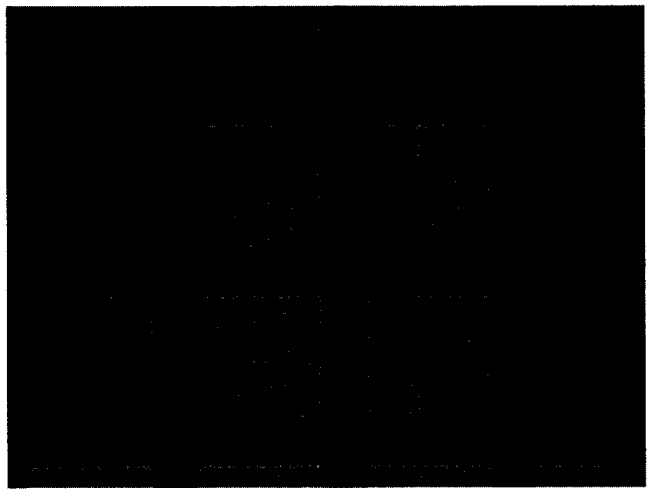

Fig. 4.3 SEM micrograph of CNTs grown on NiCr squares ($60 \times 60\ \mu m^2$).

Nano-sized metal catalyst particles are crucial for synthesis of CNTs using CVD methods. It has been demonstrated that CNT diameters are directly related to the size of catalyst particles participating in the CVD process [51]. A typical STM image of the sputtered NiCr film surface is presented in Fig. 4.4. The average grain size is around 10 nm, which can be controlled by changing the sputtering conditions, like the RF power. The grain size implies that those thicker diameter CNTs (Type A) may be grown from bigger metal grains or agglomerates of several metal grains while those thinner CNTs (Type B) may be grown from a single small grain. However, the distinct difference between the two types of CNTs in structural perfection cannot be explained only considering the sizes of the catalyst particles.

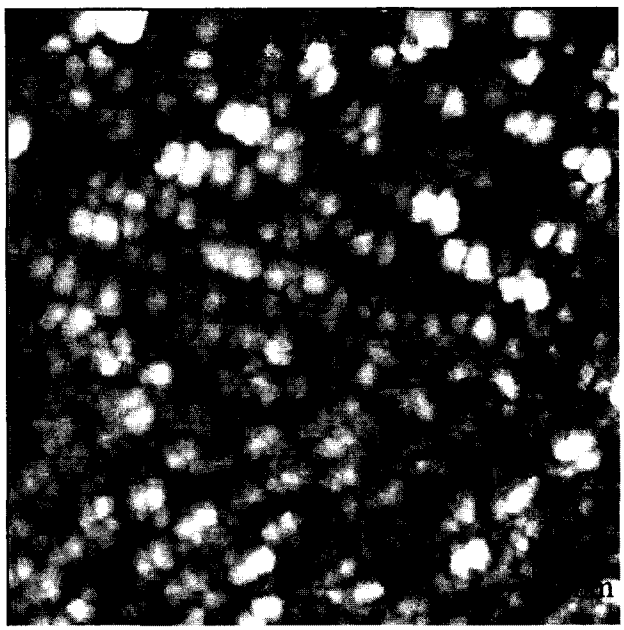

Fig. 4.4 STM image of the surface of RF sputtered NiCr film.

Raman spectroscopic analysis was also used to investigate CNT film produced by MPCVD process. A typical Raman spectrum of the CNT film is shown in Fig. 4.5 which was obtained from Fourier Transform (FT) Raman spectroscopy. Two Raman peaks appear at wave numbers of 1286 cm^{-1} and 1583 cm^{-1}, respectively. The peak at 1583 cm^{-1} is due to the strong, high frequency, in-plane stretching mode (G-mode or high energy mode (HEM)) of crystalline graphite [52], which is believed to be the structure of the CNT wall [53]. Another Raman peak at 1286 cm^{-1} is found to be deviated from the typical Raman peak of disordered graphite (D-mode), which is at 1360 cm^{-1} obtained mostly with Ar or Kr laser excitation sources [52]. The strong D-mode signal is believed to be induced by the

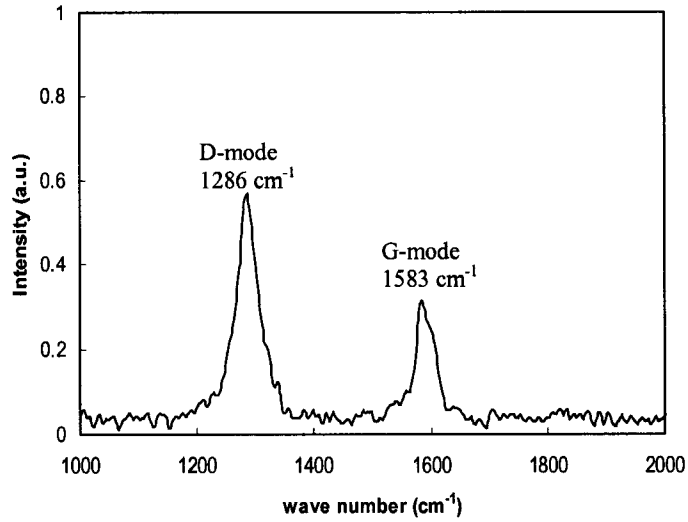

Fig. 4.5 Raman spectrum of CNT film produced by MPCVD.

carbonaceous particles, defective tube walls and ends, and finite size of the crystalline structure of nanotubes. It has been found that the disorder-activated D-mode could have a strong shift up to 50 cm^{-1}/eV due to the exciting laser photon energy [52], which could account for the observed D-mode peak shift from our sample, since we used a He-Ne laser. Similar D-mode peak shift has been shown in reference [50] for CNTs grown by MPCVD when using a 1064 nm (Nd:YAG) laser source for Raman excitation. The large intensity ratio of D-mode over G-mode from our CNT sample is also due to the small planar coherence length of the disordered graphitic material in the film, where the D/G ratio is inversely proportional to the planar coherence length over a range of 2.5-1000nm [52]. The MPCVD process used to grow CNTs is basically the same as that used for CVD diamond growth except the use of high methane concentration and metal catalyst [9]. Therefore, it is not surprising to find nano-sized carbon particles with crystalline structure included in the grown film, which would contribute to the strong D-peak in the

Raman spectrum.

4.1.3 Electron Field Emission Properties of CNTs Grown by MPCVD

A typical Field emission I-V characteristics from one CNT sample at low current level is shown in Fig. 4.6(a). The emission current increased exponentially from 2.2 nA to 49 μA as the electrical field was raised from 1V/μm to 2V/μm. Fig. 4.6(b) shows the F-N plot of the I-V curve. The straight line of F-N plot confirms that the current is due to field emission. The I-V characteristics are found to be consistent from samples prepared separately but under the same conditions. Increasing the applied field further to 4V/μm

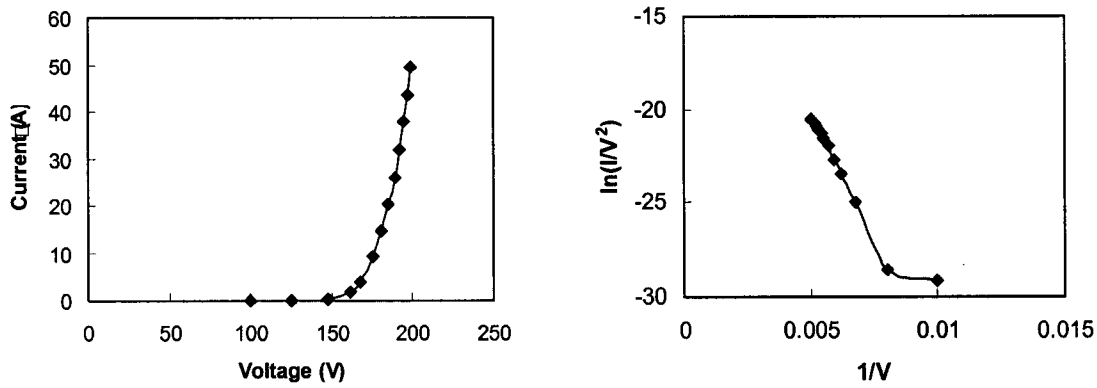

(a) (b)

Fig. 4.6 Low current level field emission from CNT film: (a) I-V plot; (b) F-N plot.

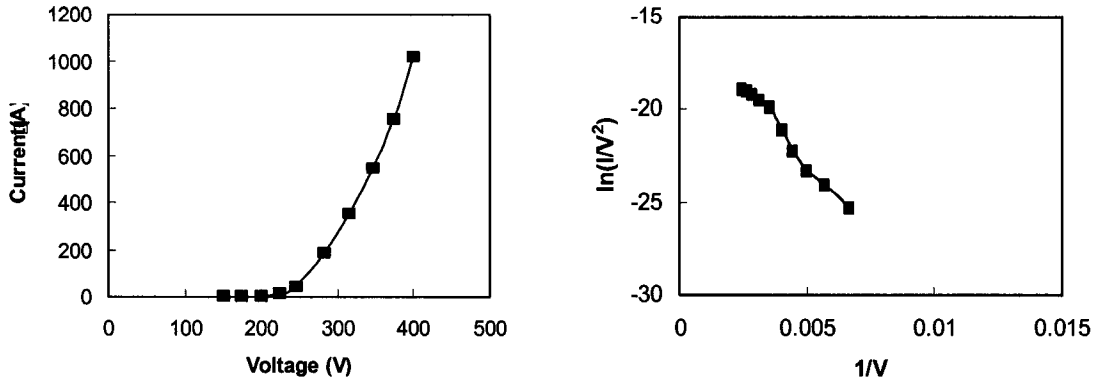

(a) (b)

Fig. 4.7 High current level field emission from CNT film: (a) I-V plot; (b) F-N plot.

raises the emission current to more than 1 mA, or an emission current density of 6.25 mA/cm^2, as shown in Fig. 4.7(a). The high current F-N plot, Fig. 4.7(b), reveals a slope change at higher field.

The low threshold for field emission from CNTs has been mainly attributed to the large field enhancement resulting from the small diameter and large aspect ratio of the tube [54]. From the slope of the F-N plot in Fig. 4.6(b) and Eqs. (2.16) and (2.18) in Chapter II, we estimate the field enhancement factor of our CNTs sample to be 5500. This value is much larger than the range of 1000-3000 which is typical of MWCNTs, but within the range of 2500-10000 which is typical of SWCNTs [55]. It is interesting that the field emission properties of our CNT samples outperform many CVD produced CNTs and are comparable to those arc-discharge and laser ablation produced CNTs which are known for good field emission performance because of their fine tube diameters and high structural quality. It has been shown that thin MWCNTs similar to our samples but produced by arc deposition, have better emission performance than both catalytically

grown open end and defective MWCNTs and SWCNTs, even though the latter ones have a much smaller tube diameter and hence larger field enhancement factor [56]. This can be considered as a result of the lack of surface states at the tube end and the screening effect of SCNT bundling [56]. Based on the comparison of the morphological and structural properties of the two types of CNTs shown in Fig. 4.1 and Fig. 4.2, we can reasonably conclude that good field emission characteristics are definitely originated from Type B CNTs with fine tube diameters and high crystalline integrity. Therefore, it will be very useful and a challenging task that the yield of Type B CNTs can be improved with more control over their length, orientation, and nucleation sites.

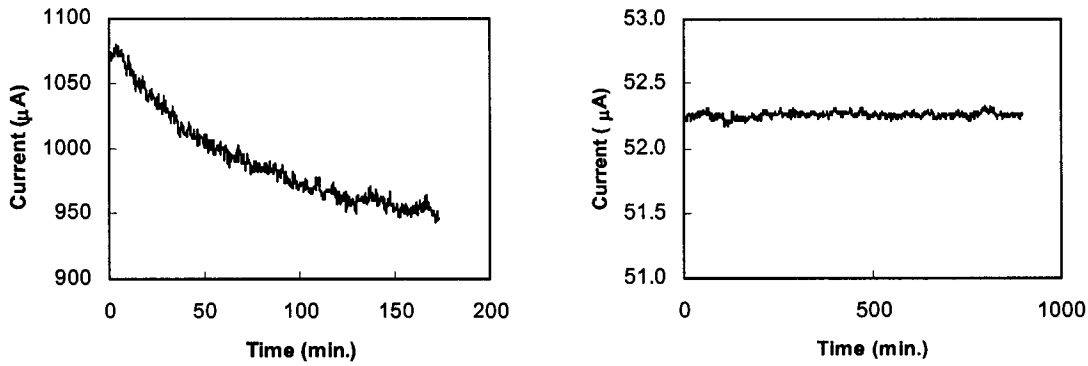

Fig. 4.8 Long-term emission stability measured at: (a) high current; and (b) low current.

The long-term emission stability was also measured at both high and low emission current levels. The results are shown in Fig. 4.9. For the high field emission, the emission current starting at 1.07 mA gradually decreases and begins to stabilize around 0.95 mA, exhibiting a 13% decrease in a 3-hr period of the stability test. The decay of the emission current is generally caused by the permanent damage due to ion bombardment from

ionized residual gas molecules, and high current density induced local heating at the emission sites. Therefore, if more high quality CNTs can be created and activated to share the current load, the emission stability will be improved. Otherwise long-term stable emission can only be achieved at low current level, like the result presented in Fig. 4.8(b) where no current decay is observed at all when the sample is emitting around 52 μA over 15 hrs. Similar to the long-term emission stability, short-term current fluctuation can also be reduced with increased emission sites because of the averaging effect.

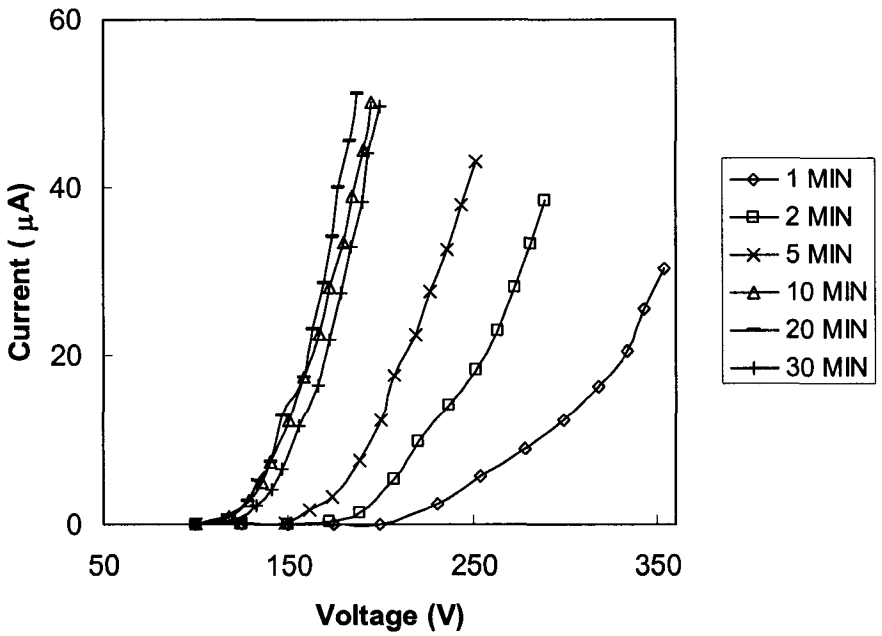

Fig. 4.9 Field emission from CNTs grown with various times.

Since it has already been known that the yield of Type B CNTs is related to growth time (see Fig. 4.1), field emission tests have been conducted on CNTs grown for various times. The field emission measurements are provided in Fig. 4.9. Qualitatively, CNT

samples grown in shorter times have higher turn-on fields than those grown in longer times. However, for samples grown in 20 and 30 min, their turn-on fields are very close to that of the 10-min sample. I-V characteristics of samples from different processing batches are both repeatable and stable in short and long term field emission tests.

Based on the experimental results presented in Fig. 4.9 and Fig. 4.1, it can be further confirmed that the field emission performance of our CNT samples are strongly correlated to the existence of the Type-B CNT CNTs. For shorter growth times, the Type-B CNTs may be too few and too short to be seen protruding from the CNT film composed of Type A CNTs and nanoparticles. Therefore, contributions from Type B CNTs to field emission are small and further subdued due to the screening effect of the higher Type-A CNTs which are poor field emitters. Otherwise, if major contribution to field emission is from Type A CNTs, there would be better emission for short time samples since the etching effect is less for Type A CNTs with shorter growth time. As the growth time increases, Type-B CNTs start protruding from the CNT film surface and consequently contribute more to the electron emission, which also decrease the turn-on field. For even longer growth time, although Type-B CNTs grow longer and more, the long CNTs start bending down due to the excessive weight, which hence reduces electron emission. The net result is only a slight decrease of the turn-on field for CNT samples grown longer than 10 minutes. It is clearly demonstrated through the above discussion that the growth of Type B CNTs is strongly dependent on the growth time that affects the field emission characteristics of those CNTs. Optimized field emission performance from CNTs can be achieved through careful control of the growth time.

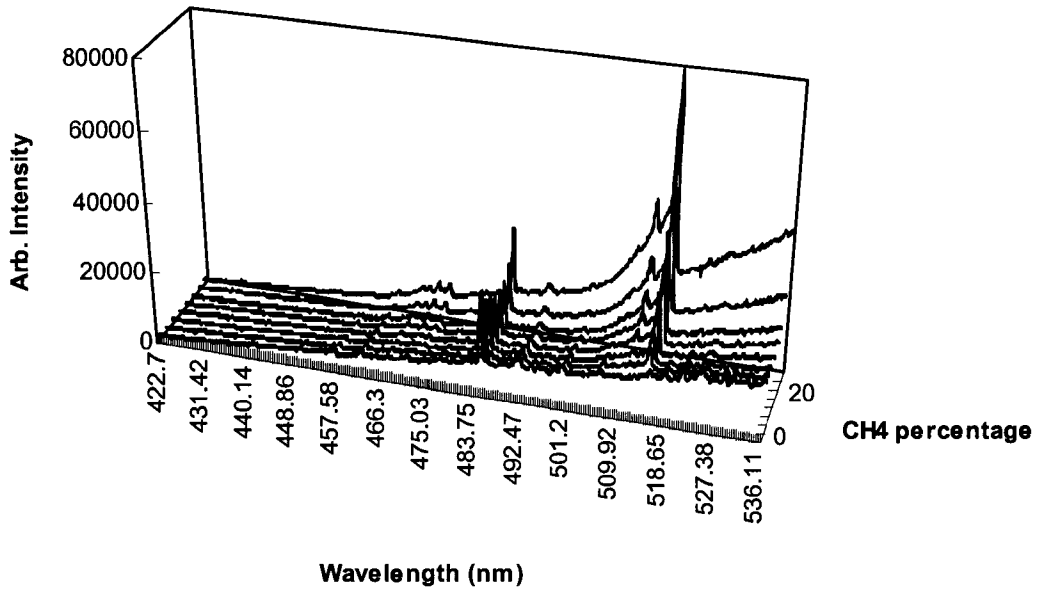

Fig. 4.10 Optical emission spectra of plasma with various methane concentrations.

Besides the growth time, we have also investigated the effect of methane concentration on the field emission performance of CNTs. Shown in Fig. 4.10 are plasma emission spectra collected at various CH_4 concentrations during the CNTs growth. The hydrogen flow is fixed at 300 sccm with a constant chamber pressure of 35 Torr during the spectrum measurement. The change of methane flow rate with a fixed hydrogen flow effectively changes the CH_4 concentration (partial pressure) and thus the carbon species in the plasma, which is the key element for CNTs growth. Two distinct peaks identified from the plasma emission spectra are C_2 (517 nm) and H_β (487 nm), which have been known to be the two key species in hydrocarbon plasma [57,58]. Those peaks have been previously found in MPCVD diamond growth with similar process conditions, where C_2 has been correlated to the higher graphite content among the diamond film [58]. As the

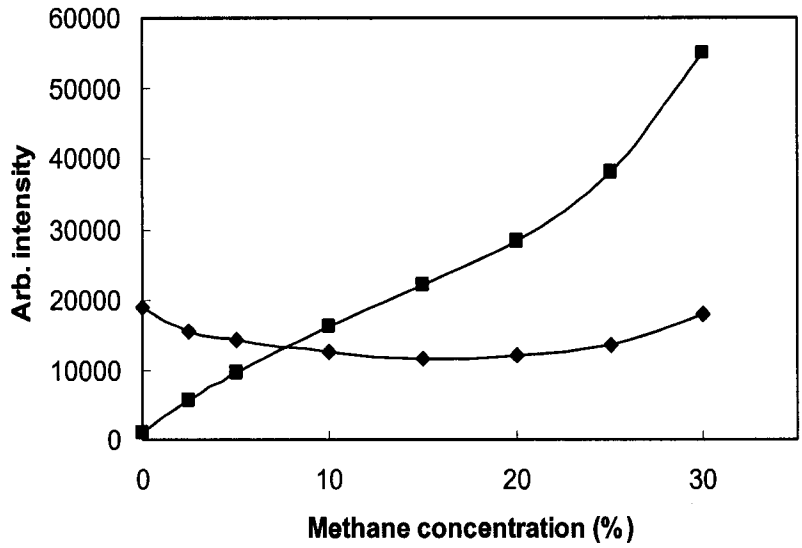

Fig. 4.11 Optical emission intensities of C_2 (square markers) and H_β (diamond markers).

CH_4 flow increases, raising up CH_4 concentration in the process chamber, the C_2 emission intensity increases steadily. However, it is interesting to see that there is an initial decrease followed by a gradual rebounding for the emission intensity of H_β with the monotonous increase of CH_4 flow rate. Shown in Fig. 4.11 are the emission intensities of C_2 and H_β at various CH_4/H_2 flow ratios, where a minimum H_β intensity is observed at a CH_4/H_2 flow ratio around 15%. Although Fig. 4.11 itself does not provide a complete picture of the CH_4/H_2 plasma chemistry, Fig. 4.11 does warrant a qualitative conclusion that CH_4, while providing carbon species for CNT growth, actually delivers more atomic hydrogen than hydrogen gas, and consequently, causes the H_β intensity to increase at a higher CH_4 concentration. This result suggests that higher hydrocarbon gas flow rate may not be helpful for CNT growth since more atomic hydrogen will be generated through plasma decomposition of the hydrocarbon gas and consequently more etching to the CNTs. CNT samples were grown in a fixed hydrogen flow of 300 sccm for

10 minutes with various CH_4 flow rates. Field emission characteristics of these CNTs samples are shown in Fig. 4.12. CNTs grown at 1% CH_4/H_2 ratio, corresponding to a high atomic hydrogen concentration (high H_β) as well as a low carbon concentration (low C_2), have the worst emission performance. However, samples grown at 5 and 10 % CH_4/H_2 ratio with lower atomic hydrogen concentration have the best field emission

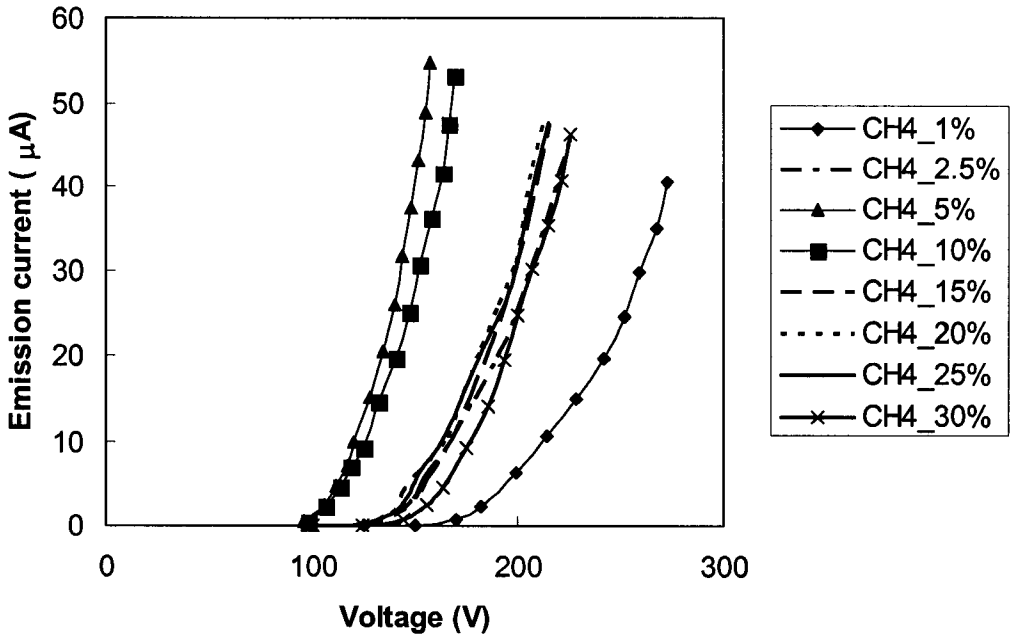

Fig. 4.12 Field emission characteristics of CNTs grown at various CH_4/H_2 flow ratios.

performance. With the carbon concentration further increasing, field emission performance degrades. This result implies that an optimal CH_4/H_2 ratio may exist producing CNTs which exhibit best field emission performance. Therefore, the correlation between the active species in hydrocarbon plasma and the field emission properties of CNTs needs further investigations.

4.2 Synthesis and Characterization of CNTs Synthesized by Thermal CVD

MWCNTs have also been successfully synthesized using atmospheric pressure thermal CVD method. Compared to MPCVD, atmospheric pressure thermal CVD experiment is much easier to conduct and the thermal CVD process is simpler too without involving plasma processes. For example, the atomic hydrogen etching effect and plasma heating do not exist in thermal CVD. In addition, it is also easier to achieve consistent growth of CNTs on Si surface, which is important for fabrication of gated CNT FEAs on Si substrates.

Furnace temperature is an important process condition which needs to be carefully determined. Since the effectiveness of catalysts is dependent on temperature, CNT growth cannot be conducted with furnace temperature blow 600 °C to avoid poor CNT yield duo to the low activeness of metal catalyst. However, furnace temperature above 800 °C is still not preferred because the formation of metal silicide can make the metal film lose its catalytic effect. In addition, lower temperatures are preferred to avoid the degradation of oxide's dielectric quality, which may lead to break-down of the oxide or large leakage current through the oxide when gate voltage is applied to start field emission. Although the gate voltage is usually not high, the electric field through the oxide is quite strong (up to 10^6 V/cm) because of the very thin (< 1 μm) oxide. Moreover, at higher temperatures, it is much easier for impurities to diffuse into the oxide to lower its dielectric strength. Therefore, the furnace temperature is generally maintained at a level between 600 °C and 700 °C.

Unlike MPCVD, acetylene is used in stead of methane as the hydrocarbon source for CNT synthesis by thermal CVD because acetylene decomposes at much lower

temperature (~ 600 °C) compared to methane (about 900 °C) so that silicide formation can be prevented and oxide quality can be maintained. The flow rate of acetylene seems to have little effect on CNT growth as long as the flow rate ratio between acetylene and the diluting gas (H_2, Ar or NH_3) is within the range of 5% - 15%. If the flow rate ratio is lower than 5%, CNT yield will become poor. If the flow ratio is higher than 15%, much more non-nanotube (amorphous carbon or graphite particles) will be deposited on the substrate surface. In addition, the flow rate ratio seems not related with the field emission performance of CNTs, which is different from the results obtained in MPCVD synthesis of CNTs.

However, three different diluting/carrier gases, H_2, Ar and NH_3, were tried for CNT synthesis, and properties of CNTs were found to be dependent on the gas mixtures. Fig. 4.13 shows the SEM and TEM micrographs of CNTs grown in the three different gas mixtures. Each gas mixture is composed of acetylene and one of the three diluting gases. The morphologies of CNTs produced by thermal CVD are very different from those produced by MPCVD. Thermal CVD produced CNTs are not straight or vertically oriented, but the tube length is longer and the number of nanotubes per unit area is lower than CNTs synthesized by MPCVD [59,60]. In addition, all CNTs shown in Fig. 4.13 appear similar to each other, which is unlike MPCVD CNTs that are composed of two distinctly different types of CNTs. The TEM pictures indicate that all samples are multi-walled CNTs. The length of CNTs is at least a few microns while the tube diameters are dependent on diluting gases used in growth. For samples grown in C_2H_2/Ar and C_2H_2/H_2, tube diameters range from 15 to 50 nm, whereas for samples grown in C_2H_2/NH_3, the tube diameters are larger ranging from 25 to 100 nm. This result may suggest that NH_3

can enhance the thermal decomposition of C_2H_2 or favor CNT nucleation on larger catalyst particles. Finally, it can be observed that both inner and outer tube diameters are irregular along the tube and defects are commonly seen, indicating lower structural quality than that of Type B CNTs but still higher than that of Type A CNTs.

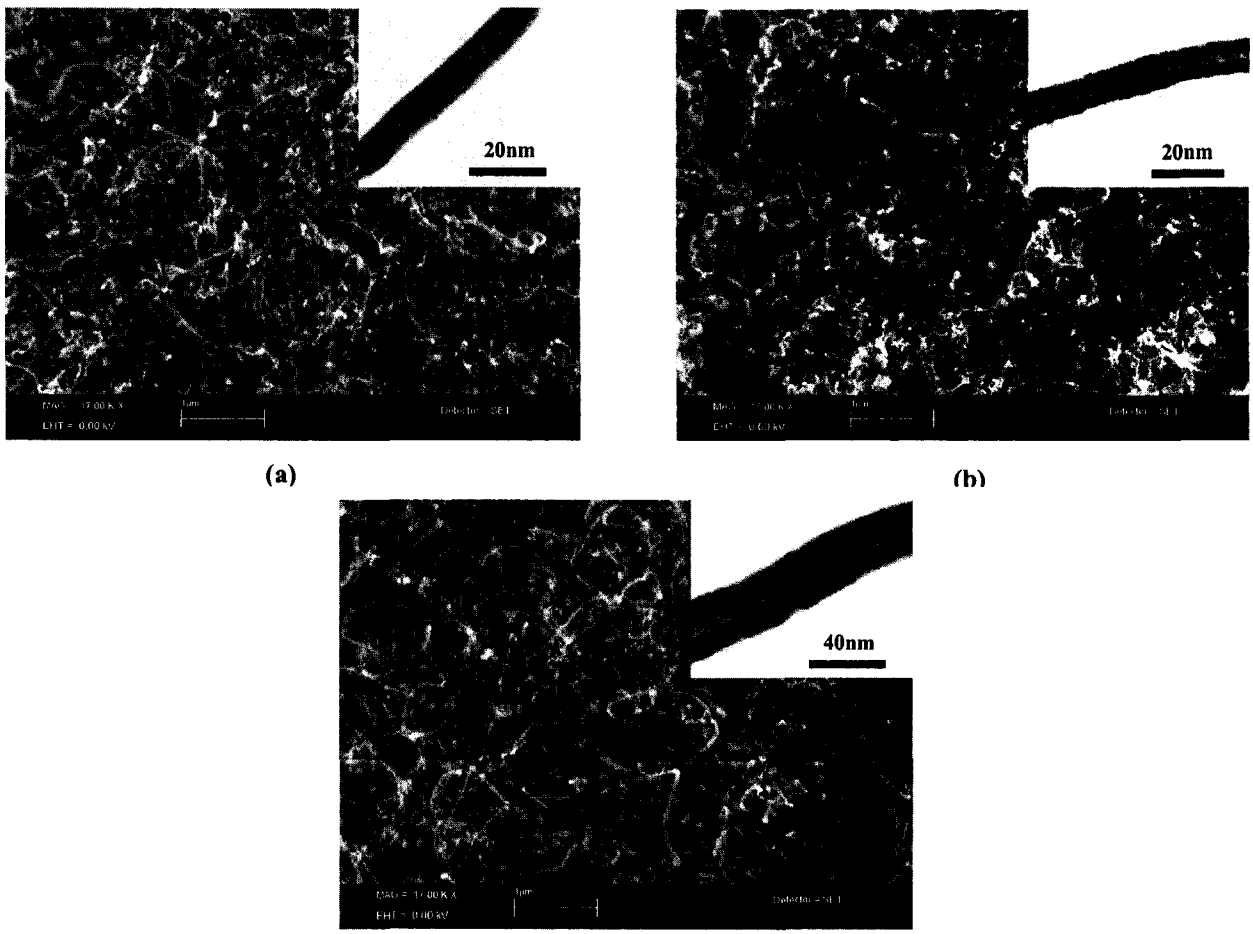

Fig. 4.13 SEM and TEM micrographs of MWCNTs grown on NiCr coated Si by thermal CVD in: (a) C_2H_2/Ar, (b) C_2H_2/H_2, and (c) C_2H_2/NH_3.

Fig. 4.14 shows a typical I-V characteristics of the field emission from CNTs. From the above discussion, it can be expected that the field emission characteristics will show

some dependence on diluting gases used in CNT growth. For samples grown in C_2H_2/Ar and C_2H_2/H_2, the turn-on field (for 1 $\mu A/cm^2$) was 2-3 V/μm and emission current density up to 10 mA/cm^2 was observed at a field of 4-5 V/μm. For samples grown in C_2H_2/NH_3, the turn-on field is higher around 3-4 V/μm and the emission current density is much lower than the other two kinds of samples. This result could be explained by considering a lower field enhancement due to larger tube diameters. The results for long-term stability tests are displayed in Fig. 4.15. Samples grown in C_2H_2/H_2 had similar results with samples grown in C_2H_2/Ar which is shown in the left graph in Fig. 4.15. The curves indicate no decay of the emission currents during the 12-hr test period. The samples grown in C_2H_2/NH_3 have a slightly larger current fluctuation than the other two kinds of samples. This could be due to the fact that samples grown in C_2H_2/NH_3 have larger tube diameters, therefore they have fewer emission sites to stabilize the emission current. The short-term current fluctuations were less than 1 percent.

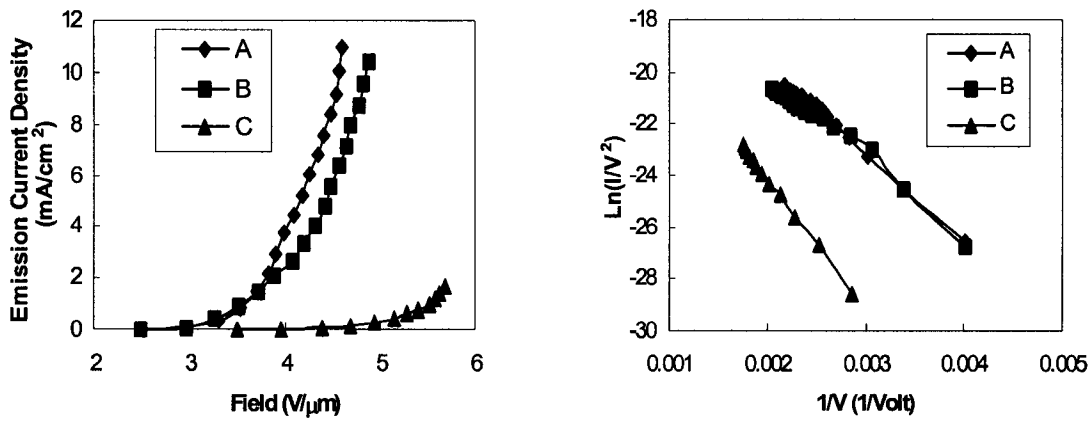

Fig. 4.14 Field emission characteristics of CNTs grown in various gas mixtures: C_2H_2+Ar (curve A); $C_2H_2+H_2$ (curve B); and $C_2H_2+NH_3$ (curve C). Left graph is the I-V plot and the right graph is the F-N plot.

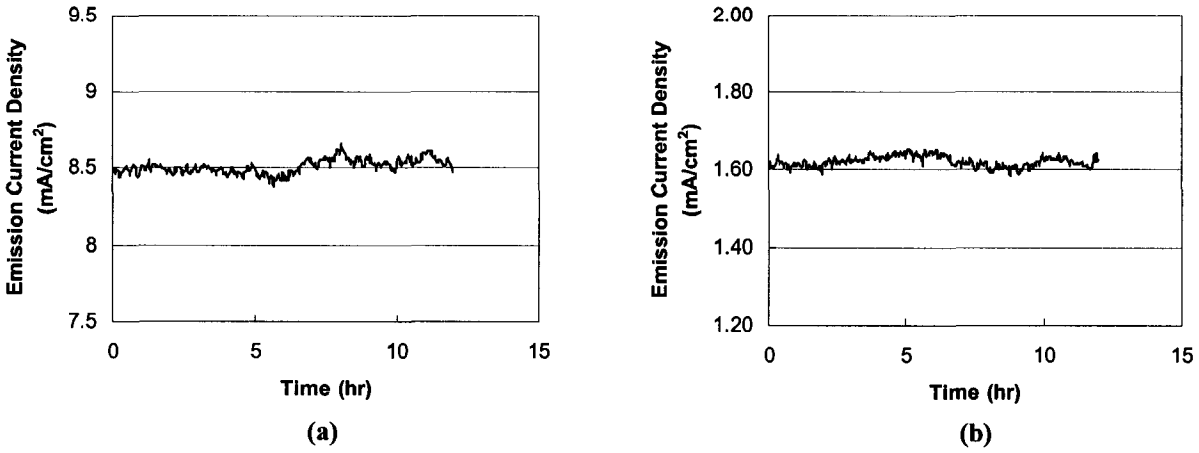

Fig. 4.15 Long-term emission stability for CNTs grown in: (a) C_2H_2/Ar, (b) C_2H_2/NH_3.

4.3 Fabrication and Field Emission of CNT FEA

4.3.1 Fabrication of Gated CNT FEAs

The gated CNT FEA structure is composed of 200 × 200 emitters. It was realized by using Si surface micromachining and thermal CVD. SEM micrographs showing a cleaved CNT FEA sample are presented in Fig. 4.16. CNTs are successfully grown at the bottom of the Si cavity, and the gate electrode is not overhanging, which is helpful to reduce the excessive collection of emission current by gate electrode. However, CNTs grown on the gate oxide can be readily observed, which may cause the FEA device to fail. The diameter of the gate hole is about 7 μm. With more advanced processing techniques, the size of gate hole can be reduced considerably, and therefore emitter density can be increased to achieve higher emission current. The non-uniform growth of CNTs can also be observed among those cavities. This certainly can result in non-uniform field emission which is major issue which limits the FEA's emission current. Therefore, a better CNT growth technique which can produce uniformly grown CNTs is really needed for fabricating CNT FEAs that can emit sufficient current for various applications.

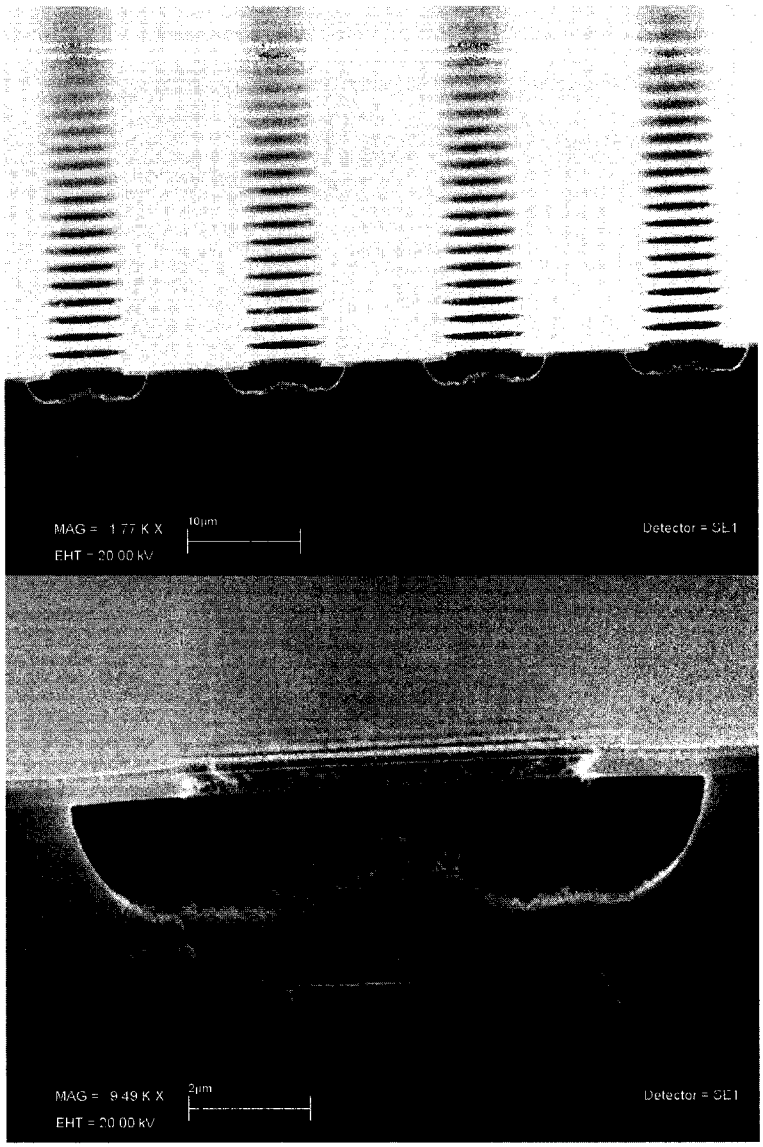

Fig. 4.16 SEM micrograph of cleaved CNT FEAs: low magnification image (top) and close-up image (bottom).

4.3.2 Field Emission Properties of Gated CNT FEAs

The field emission I-V characteristics are presented in Fig. 4.17 which is similar to published results [35,36]. The turn-on voltage is about 60 V and the F-N plot shows a straight line. The anode current is low considering the FEA is composed of 200 × 200 emitters. The low emission current is related to the morphology and quality of those

CNTs synthesized in Si cavities, which are not high quality CNTs like Type B CNTs produced by MPCVD. In addition, the emission is not uniform among the emitters because of the non-uniform growth of the CNTs in terms of length, diameter, and orientation.

In the I-V plot, gate current is not included since it is much higher than anode current. The large gate current is verified (by reversing the polarity of the gate biasing) due to a large current leakage or partial electrical breakdown through the gate insulator.

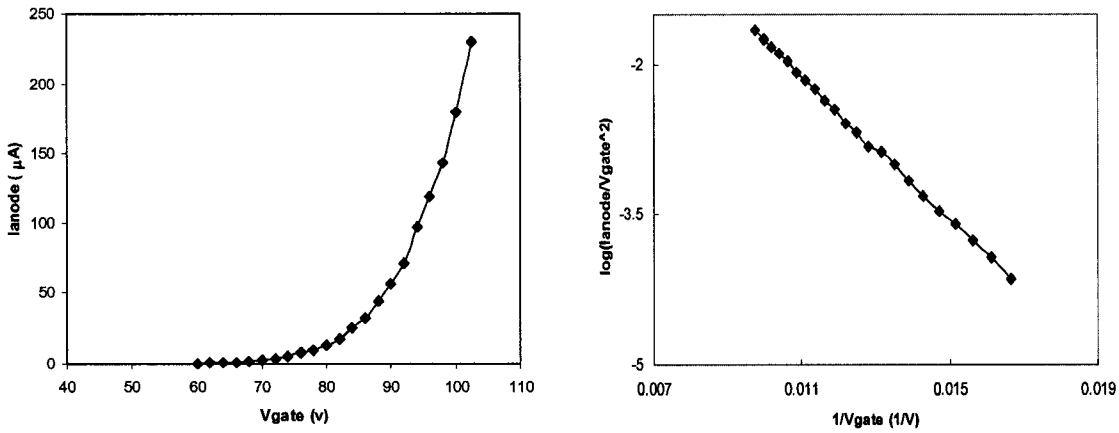

Fig. 4.17 Field emission I-V of CNT based FEAs: I-V plot (left) and F-N plot (right).

CHAPTER V

RESULTS AND DISCUSSION OF TUNGSTEN OXIDE NANORODS

In this chapter, the experimental results of the synthesis as well the structural and composition analysis of tungsten oxide nanorods are provided. The applications of nanorods in STM probes and FEAs are also demonstrated.

5.1 Synthesis and Analysis of Tungsten Oxide Nanorods

5.1.1 Synthesis of Nanorods on Tungsten Substrates

Tungsten oxide nanorods have been successfully synthesized on various tungsten substrates by thermally annealing the substrates in argon ambient at various temperatures under atmospheric pressure. No vapor source of tungsten is used. SEM micrographs of tungsten oxide nanorods grown on different tungsten substrates are shown in Fig. 5.1 for different annealing temperatures. In addition to the nanorods, nano-flakes were also grown as seen in the Fig. 5.1(d). It appears that all the nanorods have similar morphologies regardless of what substrates are used. Most of the nanorods are a few hundred nanometers long and 10 to 20 nm in diameter. However, the geometric shape of the cross section of the nanorod has not been clearly known. Due to the narrow distribution of the nanorod thickness and its high straightness (no bent or curved rods observed), it is fairly reasonable to assume that the nanorods have a cross section that is close to a circle (or a corner rounded square if considering tungsten oxide can have a cubic lattice structure or a monoclinic structure which is just slightly different from the cubic structure) which might be also ideal for the stableness of the nanorod structure. The nanorods are straight, and seem to be randomly oriented and located. Therefore, the

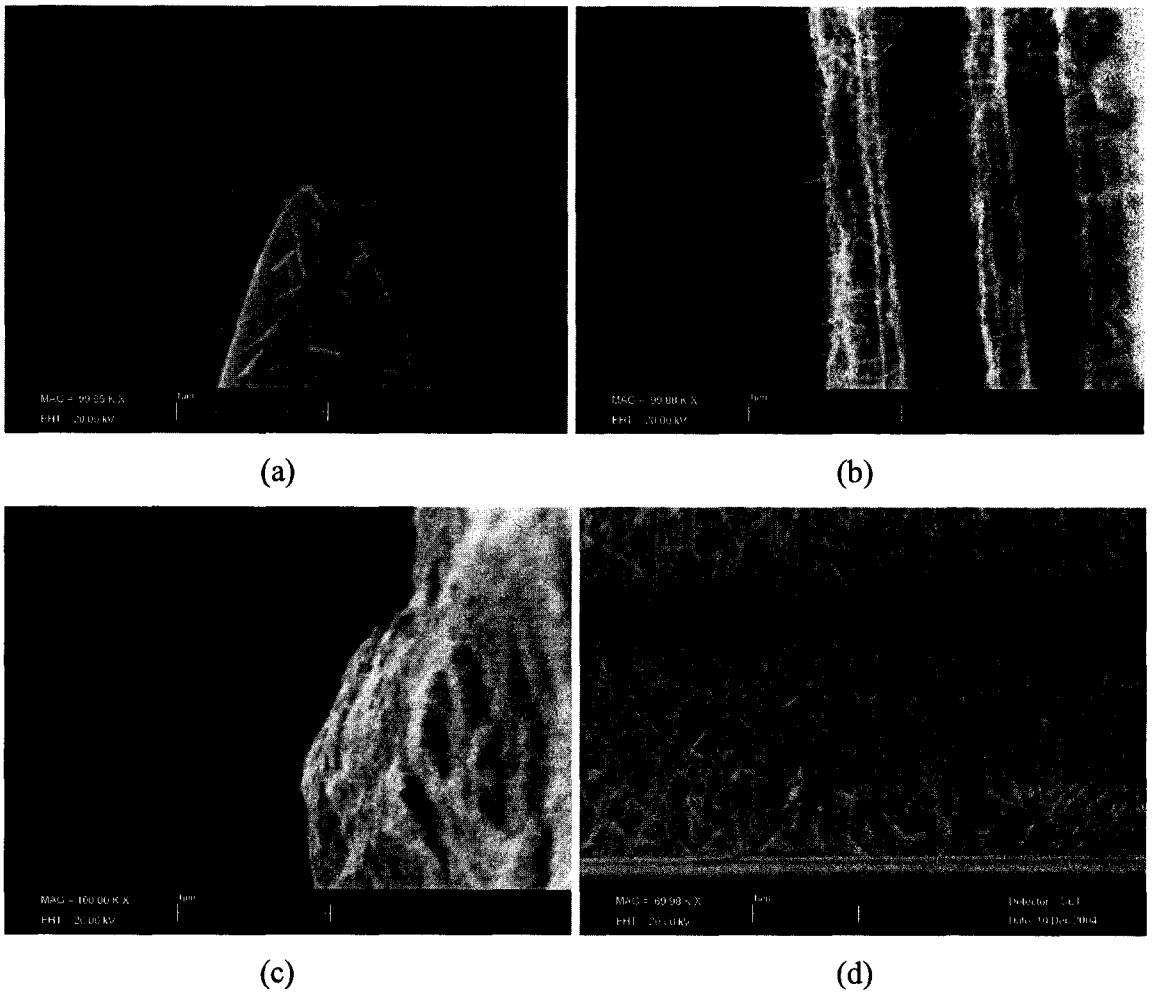

Fig. 5.1 SEM micrographs of tungsten oxide nanorods grown on various substrates with different annealing temperatures: (a) on etched tungsten tip at 750 °C; (b) on tungsten wire at 700 °C; (c) on tungsten foil at 850 °C; and (d) on RF sputtered tungsten film at 850 °C.

nucleation sites and the orientation of the nanorods might be dependent on certain local surface properties, such as defects, orientation of the surface grains, and strain on the surface. The latter may be the one of the reasons why the growth of nanorods still shows certain difference among various substrates (e.g. the yield of nanorods on tungsten foil surface is much lower than other tungsten substrates). Reference [31] reported that the shapes of tungsten nano-structures synthesized in thermal annealing were dependent on

the residual stress on the surface of sputtered tungsten film. In this dissertation work, the dependence of nanorod growth on tungsten surface condition was also observed. An electrochemically etched tungsten tip was dipped in an ultrasonically agitated diamond slurry (a nano-diamond suspension in water) for surface treatment. It was then annealed in Ar for nanorod growth. The result is shown in Fig. 5.2 in which the number density of nanorods is found to be significantly increased, but the nanorod length is very short. It is well known that dipping in diamond slurry with ultrasonic agitation is a common method for roughening a surface (adding defects/scratches). Therefore, the result shown in Fig. 5.2 can be a solid evidence demonstrating the connection between nanorod growth and tungsten surface condition which certainly needs further investigation to help fully understanding the growth mechanism of the nanorods.

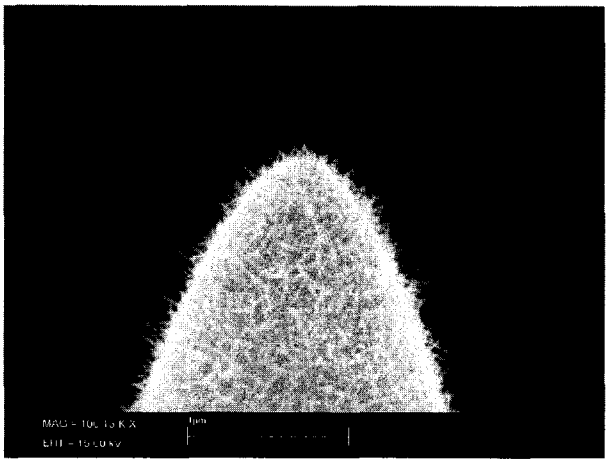

Fig. 5.2 SEM micrograph of tungsten oxide nanorods grown on tungsten tip treated in diamond slurry with ultrasonic agitation.

In order to investigate the properties of nanorod growth, various processing conditions have been applied to grow tungsten oxide nanorods. Tungsten tips were annealed in Ar ambient for various times from 2.5 min to 30 min. It is important to note that all the samples which had been annealed for various times produced very similar nanorods in terms of length and diameter. It seems that annealing time has no effect on nanorod synthesis. Reference [28] reported a similar result about tungsten nanorod synthesis, which was, explained by the authors, due to the nanorod etching caused by hydrogen. However, no hydrogen was used during the annealing process in our experiments. The same phenomenon continued to be observed even if Ar was used instead of H_2 during the temperature ramp-up process. This result will be further discussed when the nanorod growth model is proposed and discussed in the next section.

In addition to changing growth time, the effect of annealing temperatures on synthesis of nanorods on etched tungsten tips was studied. The results are shown in Fig. 5.3 in which it can be clearly found that the nanorod length increases with the annealing temperature. This result seems reasonable because higher temperatures generally can enhance the chemical reaction rate and species diffusion, which finally improves the rate of material deposition or growth.

Since it might be possible to convert tungsten oxide nanorods into other types of tungsten based nanorods, e.g. tungsten nanorods and tungsten carbide nanorods, samples were continuously annealed in H_2/Ar and C_2H_2/Ar after annealing in Ar. The extra step of annealing is intended to chemically reduce tungsten oxide back to tungsten or convert

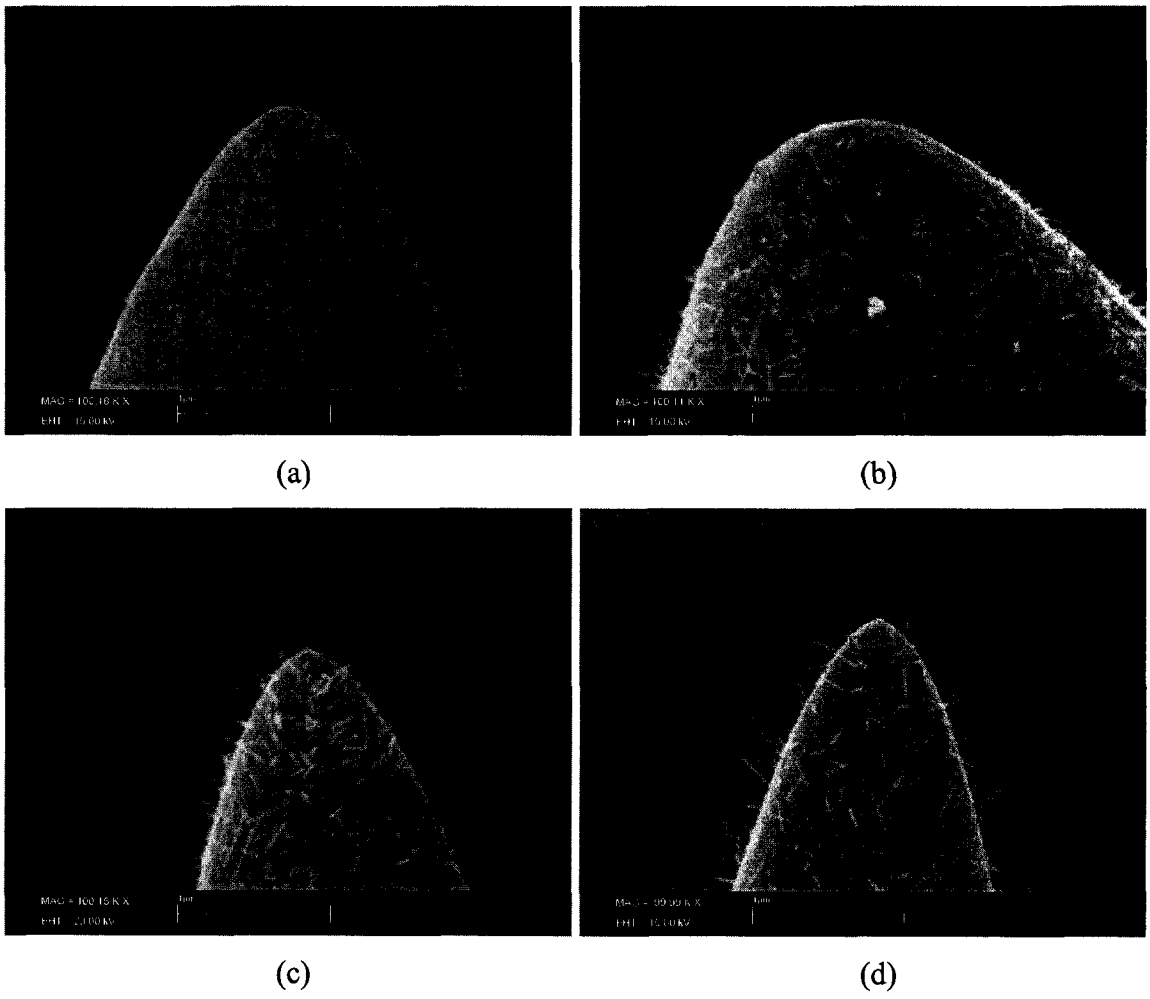

Fig. 5.3 SEM micrographs of tungsten oxide nanorods grown on tungsten tips at various annealing temperatures: (a) 650 °C; (b) 700 °C; (c) 750 °C; and (d) 800 °C.

tungsten oxide into tungsten carbide. However, those experiments were not conclusive. TEM and electron diffraction observations revealed either complete damage of the nanorods or no change in nanorod structures. However, in some HRTEM images changes are clearly observed on nanorod samples which had been annealed in C_2H_2/Ar. The changes are the extra fringes which appear on the nanorod surface (edge) and those that may be inside the nanorod. However, it cannot be determined if they are inside the

nanorod body by only observing the HRTEM images. Those extra fringes have never been observed in other samples which were not treated in C_2H_2/Ar, and have not been reported yet. However, the atomic planes that those extra fringes represent have not been determined. The results from HRTEM and EDXS (it will be given in the next section) seem to be conflicting to each other. In HRTEM images, the extra fringes look more similar to those of tungsten planes rather than the surface adsorbed layer which is mainly composed of light element compounds, like some hydrocarbon species. On the other hand, although EDXS result shows carbon signal in the spectrum, which is unlikely to create the extra fringes because of the light atomic weight of carbon. Therefore, those results may be an indication that it is possible to covert tungsten oxide nanorods into tungsten nanorods or other tungsten compound nanorods via chemical reactions in different gas ambients. This result warrants further investigation to determine the possibility for expanding the use of tungsten oxide nanorods.

5.1.2 Analysis of nanorods grown on tungsten substrates

The nanorods synthesized on tungsten tips were analyzed using HRTEM, electron diffraction and EDXS. The HRTEM images are shown in Fig. 5.4 in which fringes are observed either in parallel or perpendicular to the long axis of the nanorod. If the nanorods are composed of tungsten and other light elements, those fringes should represent atomic planes of tungsten rather than those light elements because of its large cross section of scattering. All the fringe spacings are almost identical and within the

range of 0.35 nm to 0.37 nm (these measurements are not calibrated although they are generally accurate with a few percent of errors). The HRTEM images reveal a well

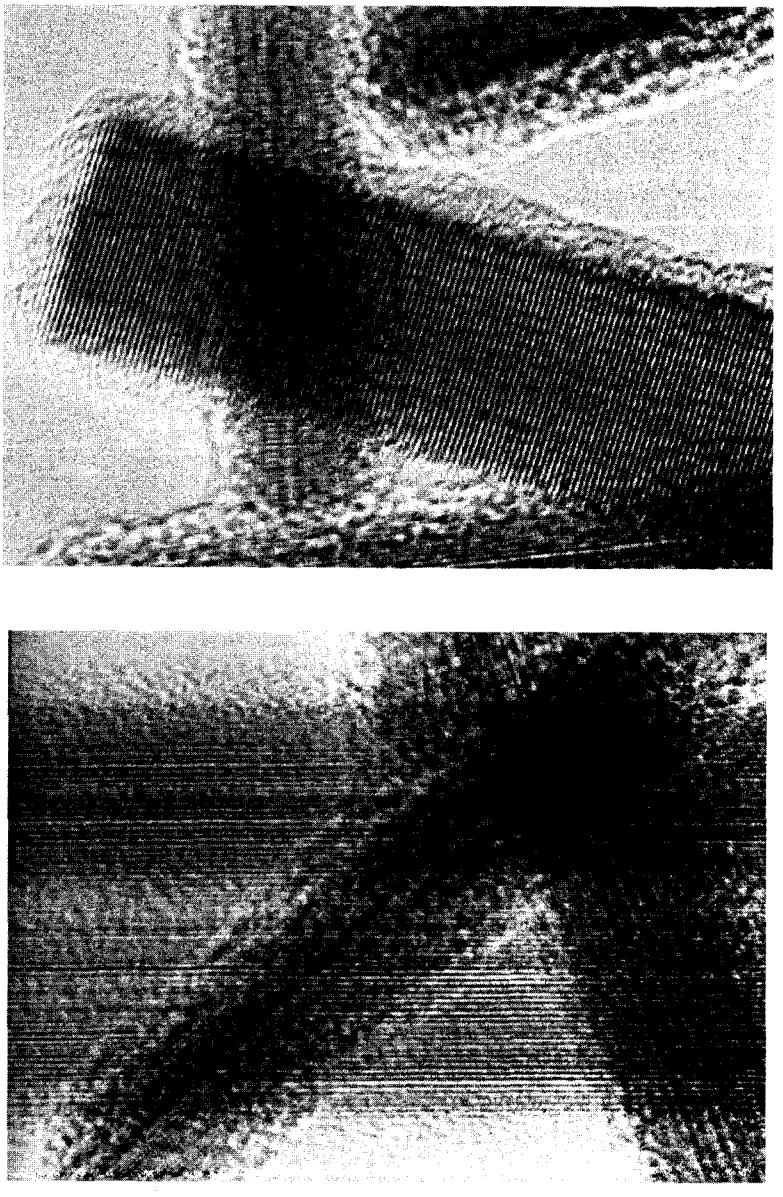

Fig. 5.4 HRTEM images of tungsten oxide nanorod.

crystallized lattice structure which could be a cubic structure or a structure very close to cubic structure. In addition to those well arranged atomic planes, an amorphous coating on nanorod surface can also be observed, which could be some radicals bonded to the nanorod surface during the nanorod synthesis process or just some gas molecules (e.g. residual gas molecules or pump oil molecules) building up on the surface during the TEM experiment.

In order to obtain more accurate information of the lattice structure of the nanorods, selected area diffraction (SAD) was performed to measure the atomic plane spacing. Typical electron diffraction pattern images are presented in Fig. 5.5, based on which atomic plane spacings can be calculated and calibrated using a gold foil diffraction pattern that was recorded under the same conditions as those for nanorods. The measured atomic plane spacings are mainly within two ranges. One of them is from 0.36 nm to 0.38 nm which is in agreement with {020} plane spacing of monoclinic WO_3 crystal, and the other is around 0.30 nm which is agreement with {112} plane spacing of monoclinic WO_3 crystal too. Both results are consistent with the published results for WO_3 nanorods that have a monoclinic structure (a = 0.7297 nm, b = 0.7539 nm, c = 0.7688 nm, and β = 90.91°) [27,61]. Based on the HRTEM and diffraction pattern images, it can be concluded that the nanorods are WO_3 with a monoclinic structure and the growth direction (the long axis of the nanorod) is along <100> direction.

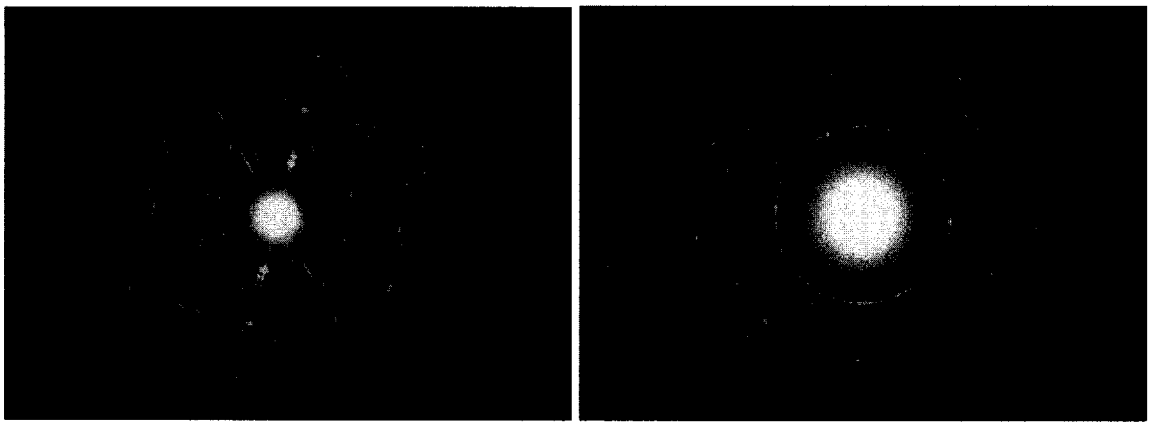

(a) (b)

Fig. 5.5 Electron diffraction patterns: (a) tungsten oxide nanorods; (b) gold film.

Except HRTEM and electron diffraction, EDXS was also conducted on nanorods to analyze their composition. A typical EDXS spectrum of nanorod sample annealed only in Ar is given Fig. 5.6(a) in which tungsten is readily detected and copper signal is also visible because of the copper grid. However, oxygen is only barely detected. Although the EDXS results cannot confirm the existence of oxygen in nanorods, it is still reasonable to claim those nanorods to be WO_3 based on the tungsten presence in nanorods, the possible species participating in the annealing, and the knowledge of the crystal structures of possible tungsten compounds. Another EDXS spectrum of nanorod sample which was first annealed in Ar and then annealed in C_2H_2/Ar is given in Fig. 5.6(b) in which carbon signal is obviously present. Since the electron diffraction pattern is still the same as that of WO_3 nanorod, it is more likely that the carbon is only deposited on the nanorod surface in amorphous form, in stead of diffusing into the nanorod and bonding with tungsten to change the lattice structure.

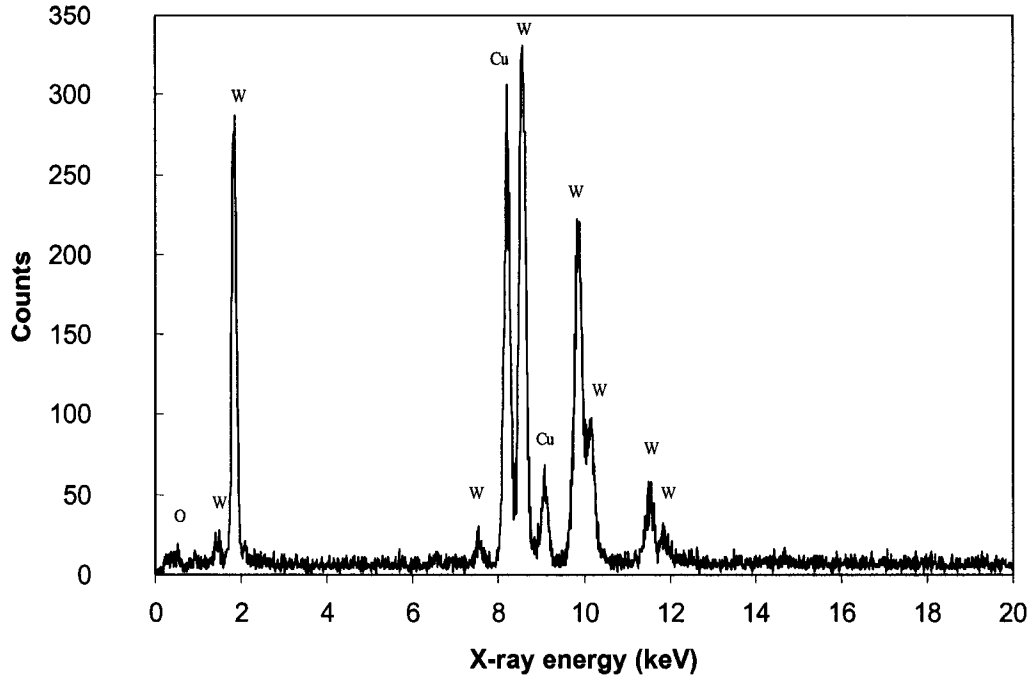

(a)

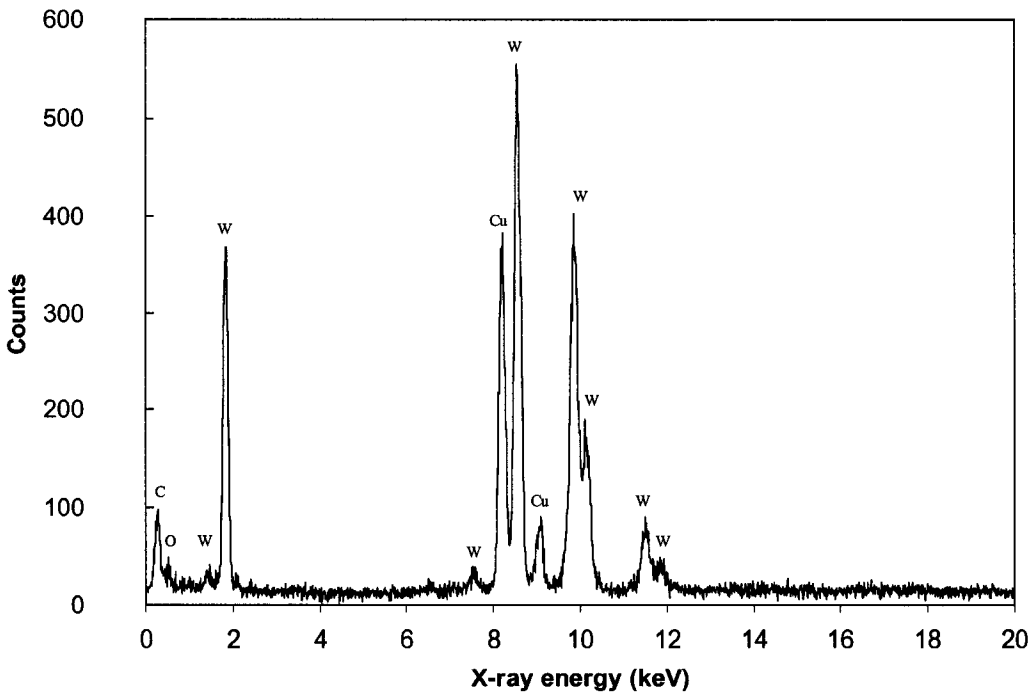

(b)

Fig. 5.6 EDXS spectra of tungsten oxide nanorods: (a) upper graph; (b) bottom graph.

5.2 Applications of Tungsten Oxide Nanorods

5.2.1 Nanorod STM probes

Nanorod STM probes were successfully fabricated by growing tungsten oxide nanorods on the apex of tungsten tips with selectively treating the apex area in diamond slurry. SEM micrographs of the nanorod STM probes are shown in Fig 5.7. Although multiple nanorods can be grown on the apex, multiple tip effect can still be avoided as long as one of the nanorods is significantly longer that others. Nanorod STM probes had been applied in STM surface imaging to obtain atomic resolution STM images on graphite surface in air under constant height mode. The STM images (raw data) are provided in Fig. 5.8 which are clean and obtained readily after only a few scans. Long time (> 1 hr) operation did not degrade the probe's performance.

5.2.2 Nanorod based FEAs

WO_3 nanorods based FEAs were successfully fabricated for the first time using the techniques described in Chapter III. SEM micrographs showing the device structure are given in Fig. 5.9. Nanorods were grown both on the gate metal and on the Si surface in the cavity. The gate hole is about 8 μm in diameter. The measured field emission I-V characteristics are illustrated in Fig. 10. The turn on voltage is about 53 V that is similar to that of CNT FEA. The device shows good performance by keeping down the gate current which is only about 5% of the anode current. However, the anode current is much lower compared to that of CNT FEA, which is very likely due to the low conductivity

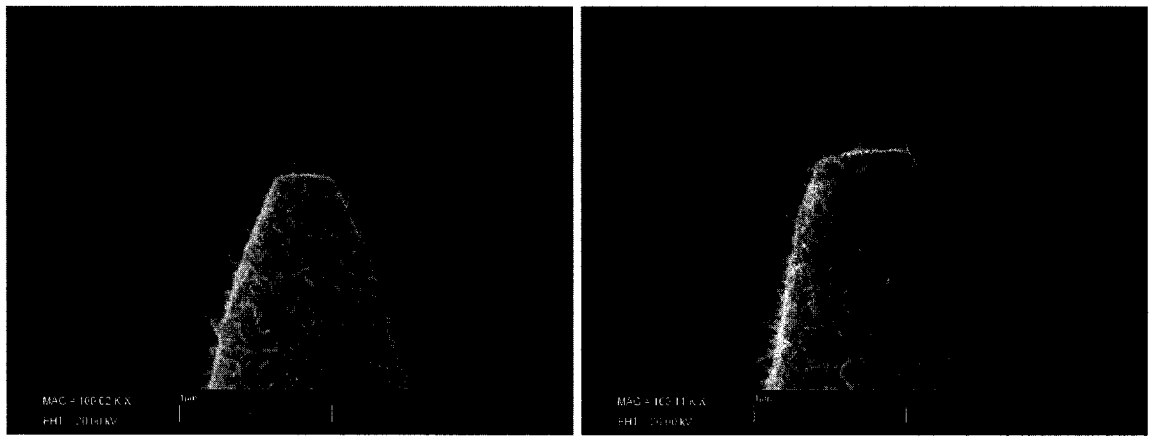

Fig. 5.7 Nanorod STM probes fabricated with selective surface treatment.

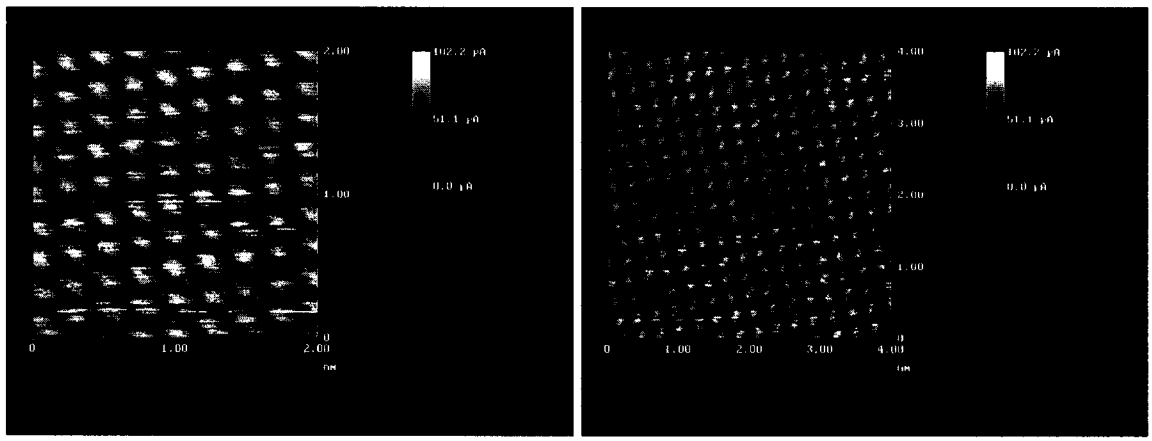

Fig. 5.8 Atomic resolution STM images of graphite surface obtained with nanorod STM probe.

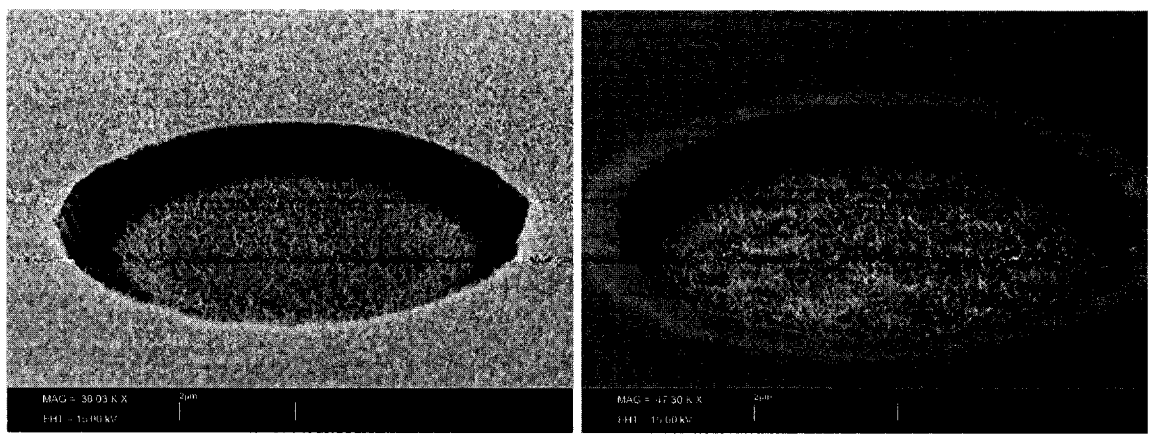

Fig. 5.9 SEM micrographs showing single field emitter with nanorods grown in the cavity.

(low electron concentration) of tungsten oxide nanorods that are only electrically semiconductive. In addition, the short length of the nanorods also limits the field enhancement. Therefore, if the tungsten oxide nanorods can be converted to tungsten or tungsten carbide nanorods and if the nanorods can be grown longer, the performance of the nanorod FEA could be enhanced considerably.

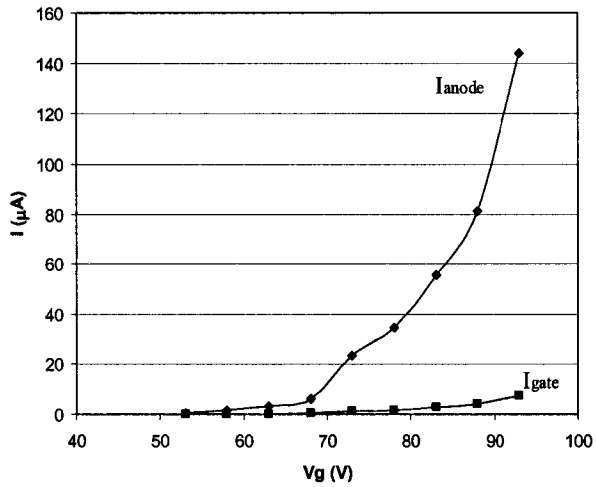

Fig. 5.10 Field emission I-V characteristics of nanorod based FEA.

CHAPTER VI

SUMMARY AND FUTURE WORK

In this chapter, the results of the research are summarized followed by suggestions for future work.

6.1 Summary of the Dissertation Work

This dissertation work mainly focused on the synthesis and field emission properties of CNTs and tungsten trioxide nanorods as well as their applications in FEAs and STM probes.

CNTs synthesis was achieved using both MPCVD and thermal CVD. High quality vertically-aligned MWCNTs were discovered in CNT films produced on SiO_2 by MPCVD, and those CNTs exhibit good performance in field emission. The field emission characteristics were found dependent on growth time and methane concentration. Thermal CVD was implemented to grow CNTs in FEAs because CNTs could not be synthesized on Si or metal surface by MPCVD. CNTs grown by thermal CVD had similar field emission performance as those grown by MPCVD. CNTs were successfully synthesized in the Si cavities of the gated FEAs which were fabricated via Si micromachining techniques. Field emission with low turn-on voltage was achieved from CNTs based FEAs.

Single-crystalline tungsten oxide nanorods were successfully synthesized on various tungsten substrates via thermal annealing in Ar ambient. Their lattice structure and composition were analyzed using various analysis techniques. The nanorod growth mechanism was proposed based on two effects: (a) thermal oxidation of tungsten in an ambient with very low partial pressure of oxygen, which produces volatile tungsten oxide

species; and (b) self-catalytic effect that enable volatile oxide species to nucleate and grow from certain surface sites. Tungsten oxide nanorods were grown on tungsten tips for application in STM as probes, and they were also successfully grown in FEA cavities for application in electron field emission. Both applications have shown promising performance.

6.2 Suggestions for Future Work

Promising applications of those investigated nanomaterials have been successfully demonstrated. However, the fabrication and performance of those devices still need to be improved. For instance, high quality CNTs need to be synthesized with precise control over the length, diameter and number density of CNTs. Therefore, large number of such CNTs will emit simultaneously to obtain stable and high emission current density as well as long life time. Recently, high quality SWCNTs or MWCNTs were readily and uniformly synthesized from metal particles embedded in porous ceramic materials via simple thermal CVD process [62]. The CNT diameter and number density could be tuned by changing the amount of metal salt that was put into the ceramic matrix. This CNT synthesis method could be used to grow high quality CNTs in FEAs to achieve high emission current if the ceramic materials can be made electrically conductive. Similarly, the synthesis of tungsten oxide nanorods needs to be optimized based on the requirements mentioned above. Conversion of tungsten oxide nanorods into other tungsten based nanorods could be interesting and more useful because tungsten oxide has limited conductivity and modest melting point which make it undesirable for many applications. In addition, the same or similar nanorod growth method may be applied to other materials so that more nanorod materials can be obtained leading to various promising applications.

REFERENCES

[1] K. R. Shoulders, *Adv. Comp.* **2**, 135 (1961).

[2] C. Spindt, *J. Appl. Phys.* **39**, 3504 (1968).

[3] I. Brodie and C. A. Spindt, Vacuum microelectronics, in *Advances in Electronics and Electron Physics*, vol. 83 (P. W. Hawkes, Ed.), Academic Press: New York, p. 1 (1992).

[4] W. B. Choi *et al.*, *Jpn. J. Appl. Phys.* **39**, 2560 (2000).

[5] H. F. Gray, G. J. Campisi, and R. F. Greene, A vacuum field effect transisitor using silicon field emission arrays, in *Technical Digest of IEDM*, Washington, D.C., 776 (1986).

[6] C. P. Spindt, C. E. Holland, P. R. Schwoebel, and I. Brodie, Field-emitter-array development for microwave application (II), in *Proc. 10th IVMC*, Kingju, Korea, 200 (1997).

[7] S. Kaneman, K. Ozawa, K. Ehara, T. Hirano, and J. Itch, MOSFET-structured Si field emitter tip, in *Proc. 10th IVMC*, Kingju, Korea, 34 (1997).

[8] J. Itoh, T. Hirano, and S. Kanemaru, *Appl. Phys. Lett.* **69**, 1577 (1996).

[9] S. Albin, W. Fu, A. Varghese, and A. C. Lavarias, *J. Vac. Sci. Technol. A* **17**, 2104 (1999).

[10] W. P. Kang, T. Fisher, and J. L. Davidson, *New Diamond and Frontier Carbon Technology* **11**, 129 (2001).

[11] J. Itoh, *Appl. Surf. Sci.* **111**, 194 (1997).

[12] C. O. Bozler, C. T. Harris, S. Rabe, D. D. Rathman, M. A. Hollis, and H. I. Smith, *J. Vac. Sci. Technol. B* **12**, 629 (1994).

[13] C. A. Spindt, C. E. Holland, and R. D. Stowell, *Appl. Surf. Sci.* **16**, 268 (1983).

[14] S. Iijima, *Nature* **354**, 56 (1991).

[15] T. W. Odom, J.-L. Huang, P. Kim, and C. M. Lieber, *J. Phys. Chem. B* **104**, 2794 (2000).

[16] W. Liang *et al.*, *Nature* **411**, 665 (2001).

[17] S. P. Frank, P. Poncharal, Z. L. Wang, and W. A. de Heer, *Science* **280**, 1744 (1998).

[18] P. Kim, L. Shi, A. Majumdar, P. L. McEuen, *Phys. Rev. Lett.* **87**, 215502 (2001).

[19] E. W. Wong, P. E. Sheehan, C. M. Lieber, *Science* **277**, 1971 (1997).

[20] N. S. Lee *et al.*, *Diamond Relat. Materials* **10**, 265 (2001).

[21] Y. Saito, S. Uemura, *Carbon* **38**, 169 (2000).

[22] R. Rosen *et al.*, *Appl. Phys. Lett.* **76**, 1668 (2000).

[23] H. Sugie *et al.*, *Appl. Phys. Lett.* **78**, 2578 (2001).

[24] R. H. Baughman, A. A. Zakhidov, and W. A. de Heer, *Science* **297**, 787 (2002).

[25] H. Dai, E. W. Wong, Y. Z. Lu, S. Fan, and C. M. Lieber, *Nature* **375**, 769 (1995).

[26] T. Arie, S. Akita, and Y. Nakayama, *J. Phys. D: Appl. Phys.* **31**, L49 (1998).

[27] Y. Q. Zhu, W. Hu, W. K. Hsu, M. Terrones, N. Grobert, J. P. Hare, H. W. Kroto, D. R.M.Walton, and H. Terrones, *Chem. Phys. Lett.* **309**, 327 (1999).

[28] Y.-H. Lee, C.-H. Choi, Y.-T. Jang, E.-K. Kim, B.-K. Ju, N.-K. Min, and J.-H. Ahn, *Appl. Phys. Lett.* **81**, 745 (2002).

[29] G. Gu, B. Zheng, W. Q. Han, S. Roth, and J. Liu, *Nano Lett.* **2**, 849 (2002).

[30] S.-J. Wang, C.-H. Chen, S.-C. Chang, K.-M. Uang, C.-P. Juan, and H.-C. Cheng, *Appl. Phys. Lett.* **85**, 2358 (2004).

[31] Y.-H. Lee, D.-H. Kim, C.-H. Choi, Y.-T. Jang, and B.-K. Ju, *Appl. Phys. Lett.* **85**, 5977 (2004).

[32] K. Liu, D. T. Foord, and L. Scipioni, *Nanotechnology* **16**, 10 (2005).

[33] I. Matsubara *et al.*, *Jpn. J. Appl. Phys.* **28**, L1121 (1989).

[34] R. Funahashi, I. Matsubara, and M. Shikano, *Chem. Mater.* **13**, 4473 (2001).

[35] D. S. Y. Hsu, J. Shaw, *Appl. Phys. Lett.* **80**, 118 (2002).

[36] I. T. Han *et al.*, *Appl. Phys. Lett.* **81**, 2070 (2002).

[37] R. H. Fowler and L. W. Nordheim, *Proc. R. Soc.* (London) **A119**, 173 (1928).

[38] S. O. Kasap, *Principles of Electrical Engineering Materials and Devices*, McGraw-Hill, New York (1997).

[39] I. Brodie and P. R. Schwoebel, *Proceedings of the IEEE* **82**, 1006 (1994).

[40] R. H. Good and E. W. Muller, in *Handbuch der Physik*, edited by Springer-Verlag (Berlin, Germany, 1956), Vol. **21**, p. 176.

[41] C. A. Spindt, I. Brodie, L. Humphrey, and E. R. Westerberg, *J. Appl. Phys.* **47**, 5248 (1976).

[42] I. Brodie, and C. A. Spindt, in *Advances in Electronics and Electron Physics*, edited by P. W. Hawkes, Academic Press (San Diego, 1992), Vol. **83**, p. 2.

[43] G. Binnig, H. Rohrer, Ch. Gerber, and E. Weibel, *Phys. Rev. Lett.* **49**, 57 (1982).

[44] N. Garcia, C. Ocal, and F. Flores, *Phys. Rev. Lett.* **50**, 2002 (1983).

[45] E. Stoll, A. Baratoff, A. Selloni, and P. Carnevali, *J. Phys. C* **17**, 3073(1984).

[46] N. D. Lang, *Phys. Rev. B* **36**, 8173 (1987).

[47] N. D. Lang, A. Yacoby, and Y. Imry, *Phys. Rev. Lett.* **63**, 1499 (1989).

[48] J. Bardeen, *Phys. Rev. Lett.* **6**, 57 (1961).

[49] C. Bower *et al.*, *Appl. Phys. Lett.* **77**, 830 (2000).

[50] Y. C. Choi *et al.*, *J. Appl. Phys.* **88**, 4898 (2000).

[51] Y. C. Choi *et al.*, *Appl. Phys. Lett.* **76**, 2367 (2000).

[52] J. R. Dennison, M. Holtz, and G. Swain, *Spectroscopy* **11**, 38 (1996).

[53] H. Hiura *et al.*, *Chem. Phys. Lett.* **202**, 509 (1993).

[54] Y. Saito and S. Uemura, *Carbon* **38**, 169 (2000).

[55] J. M. Bonard, *et al.*, *Appl. Phys. Lett.* **73**, 918 (1998).

[56] J. M. Bonard, *et al.*, *Appl. Phys. A* **69**, 245 (1999).

[57] G. Balestrino, M. Marinelli, E. Malani, A. Paoletti, I. Pinter, A. Tebano, and P. Proli, *Appl. Phys. Lett.* **62**, 879 (1993).

[58] W. Fu, A. Lavarias, and S. Albin, presented at 52th Annual Gaseous Electronics Conference, Oct. 5-8, Norfolk, Virginia, USA, 1999.

[59] Y. J. Yoon and H. K. Baik, *J. Vac. Sci. Technol. B* **19**, 27 (2001).

[60] J. I. Sohn *et al.*, *Appl. Phys. Lett.* **78**, 901 (2001).

[61] PDF database: card number 43-1035, space group P21/n.

[62] Y. Zhang *et al.*, *Appl. Phys. Lett.* **79**, 3155 (2001).

VITA

Bing Xiao

4707 Killam Ave, Apt. A2
Norfolk, Virginia 23508
USA

Bing Xiao was born in Chengdu, Sichuan Province, People's Republic of China, in December 1968. He received his B.S. degree in Semiconductor Physics and Devices in 1990 and M.S. degree in Condensed Matter Physics in 1993. Both degrees were obtained at Sichuan University, Chengdu, P. R. China. From 1993 to1998, he worked as an instructor at the Department of Microelectronic Science and Engineering in University of Electronic Science and Technology of China, Chengdu, China. Since 1998, he has been a PhD student majoring in electrical engineering with the Department of Electrical and Computer Engineering at Old Dominion University, Norfolk, Virginia. He has authored and co-authored 10 journal papers and 5 conference articles. His research interests include semiconductor devices, micro-fabrication, vacuum microelectronic devices, and nanomaterials.